J. Fluid Mech. (2005), *vol.* 529, *pp.* 279–310.
doi:10.1017/S0022112005003599 Printed in the United Kingdom

Kinematics and depth-integrated terms in surf zone waves from laboratory measurement

By PETER K. STANSBY[1] AND TONG FENG[2]

[1]School of Mechanical, Aerospace and Civil Engineering, University of Manchester, Manchester M60 1QD, UK

[2]Department of Aeronautical and Automotive Engineering, Loughborough University, Loughborough LU11 3TU, UK

(Received 10 April 2003 and in revised form 14 December 2004)

Kinematics of nominally periodic surf zone waves have been measured in the laboratory using LDA (laser Doppler anemometry), above trough level as well as below, for weakly plunging breakers transforming into bores in shallower water. The aim was to determine, through phase- or ensemble-averaging, periodic flow structures in a two-dimensional vertical plane, from large-scale down to small-scale vortical structures. Coherent multiple vortical structures were evident at the initiation of breaking, becoming elongated along the surface during bore propagation. The initial region is likely to become more extensive as waves become more strongly plunging and could explain the difference in turbulence characteristics between plunging and spilling breakers observed elsewhere. Comparison of vorticity magnitudes with hydraulic-jump measurements showed some similarities during the initial stages of breaking, but these quickly grew less as breaking progressed into shallower water. Period-averaged kinematics and vorticity were also obtained showing shoreward mass transport above trough level and undertow below, with a thick layer of vorticity at trough level and a thin layer of vorticity of opposite rotation at the bed. There were also concentrated regions of mean vorticity near the end of the plunging region. Residual turbulence of relatively high frequency was presented as Reynolds stresses, showing marked anisotrophy. Dynamic pressure (pressure minus its hydrostatic component) was determined from the kinematics. The magnitudes of different effects were evaluated through the depth-integrated Reynolds-averaged Navier–Stokes (RANS) equations, which may be reduced to nine terms (the standard inviscid terms of the shallow-water equations conserving mass and momentum with hydrostatic pressure, and six additional terms), assuming that the complex, often aerated, free surface is treated as a simple interface. All terms were evaluated, assuming that a space/time transformation was justified with a slowly varying phase speed, and the net balance was always small in relation to the maxima of the larger terms. Terms due to dynamic pressure and vertical dispersion (due to the vertical variation of velocity) were as significant as the three terms in the inviscid shallow-water equations; terms involving residual turbulence were insignificant. The r.m.s. (root mean square) variation of each along the slope is highly irregular, with the inertia term due to (Eulerian) acceleration always greatest. This is consistent with complex, though repetitive, coherent structures. Modelling the flow with the shallow-water equations, using the surface elevation variation at the break point as input, nevertheless gave a good prediction of the wave height variation up the slope.

1. Introduction

The hydrodynamics of breaking waves in the surf zone has been the subject of considerable research owing to the complexity of the physical processes and their importance in determining cross-shore and alongshore sediment transport, the resulting beach profiles, and overtopping and flooding of dunes and sea defences. Measurements of water surface elevation giving wave heights, set-down and set-up have been made for many situations, including plane slopes and bars (e.g. see Madsen, Sorensen & Schäffer 1997). Comparison with hydraulic jumps is quite natural as the one-dimensional inviscid problem is identical to that of a bore in the frame of reference moving with the bore. Peregrine & Svendsen (1978) observe that vorticity is generated at the toe of the roller which is initially similar to a mixing layer. Yeh & Mok (1990) compared the hydraulic jump with an isolated bore and found differences due to different shear layers at the bed resulting from different boundary conditions. They also observed, for low Froude numbers of interest here (less than about 2), coherent structures generated at the toe of the roller with an apparently different nature from those of mixing layers. Detailed measurements of the kinematics and turbulence in hydraulic jumps with detailed analysis have been made by Svendsen *et al.* (2000). Nadaoka, Hino & Koyano (1989) measured turbulence structures under periodic spilling breakers propagating over a horizontal bed, using laser Doppler anemometry (LDA). They showed the existence of multiple horizontal vortices (coherent vortical structures), shoreward of a crest, and intense obliquely descending vortices, seaward of a crest. The latter are inclined vortices in a vertical plane which have been identified as occurring intermittently for a small proportion of the time, about 2 %, while making a significant contribution to average turbulence intensity, about 20 %, in spilling breakers (Cox & Kobayashi 2000). In plunging breakers these proportions are about 7 % and 40 %, respectively (Cox & Anderson 2001). The formation mechanism remains elusive. Ting & Kirby (1994, 1995, 1996) have made turbulence measurements in the surf zone, below trough level, under plunging and spilling breaking waves. They could only measure the horizontal and vertical components of velocity independently and paid particular attention to the transport of turbulent kinetic energy, which was transported landward under plunging breakers with dissipation within one wave cycle and was transported seaward under spilling breakers with much slower dissipation. Cowen *et al.* (2003) have measured turbulence, including Reynolds stresses, in the swash zone using PIV (particle image velocimetry) and showed that the swash flows forced by plunging and spilling breakers are similar. In addition to complex kinematics and turbulence, breaking waves also entrain air, generating a two-phase flow (three-phase if sediment is entrained), which is scale and salinity dependent. Finally, the surf zone in reality results from offshore waves, which are random to some degree.

The practical importance of these flows has encouraged numerical modelling. The most general approach is probably through the solution of the Navier–Stokes equations in VOF (volume of fluid) form to accommodate the free surface: in a two-dimensional vertical plane using sophisticated turbulence modelling, e.g. Lin & Liu (1998), or in three-dimensional using LES (large eddy simulation), e.g. Christiansen & Deigaard (2001) who qualitatively reproduce the inclined vortices mentioned above. Such general approaches are particularly valuable for predicting interaction with steep coastal structures, but are prohibitively computationally demanding for large-scale three-dimensional problems, and are likely to remain so for the foreseeable future even with the present rate of increase of computer power.

Numerical methods with a much longer history are based on the depth-averaged shallow-water equations, derived from the Navier–Stokes equations assuming hydrostatic pressure. The lack of frequency dispersion causes any initially smooth wave profile to steepen as it propagates, to form a shock or bore. While this is clearly not representative of an irrotational wave, it has been used to represent spilling breakers in the surf and swash zones with some success. Early work relied on resolving the flow parallel to the slope (Hibberd & Peregrine 1979) while later methods have successfully applied methods developed for compressible aerodynamics, particularly Riemann solvers as described in Toro (2001), also Dodd (1998) for practical applications. These methods essentially conserve mass and momentum and represent the bore as a sharp interface without spurious oscillations. The shallow-water equations have been extended to approximate dispersive, irrotational waves through additional terms as the Boussinesq equations, originally for shallow-water waves (Peregrine 1967). Since then there has been considerable effort in extending these equations to be valid for intermediate- and now deep-water waves, e.g. Madsen, Bingham & Liu (2002). These methods are highly efficient as one-dimensional solutions and are suited for practical computations in two-dimensions on modern PCs. Various breaker models have been suggested to close the solution from initial breaking to bore formation in shallower water. Models of the roller type, assuming a volume of water moving at the wave speed with a geometry based on hydraulic jump knowledge, have been used by Schäffer, Madsen & Deigaard (1993) and Madsen *et al.* (1997). Another model (Zelt 1991) assumes that the breaker may be represented as a diffusion term with various empirical criteria, conserving momentum while dissipating energy. This was applied to solitary waves and has been developed for periodic waves by Kennedy *et al.* (2000) with further empirical modification. A model involving the solution of the vorticity equation has been suggested by Veeramony & Svendsen (2000), using the hydraulic jump results of Svendsen *et al.* (2000). All models require some empirical definition for the onset of breaking. Wave height and set-up have been compared with experiment, and predictions by the Boussinesq equations with breaker models are somewhat mixed, being generally poor around the initiation of breaking and requiring different empirical 'constants' for different situations. An original intention of the present work was to evaluate the terms in the depth-integrated Reynolds-averaged Navier–Stokes (RANS) equations through physical experiment to inform the modelling of rollers within the nonlinear shallow-water equations or the Boussinesq equations.

The underlying physical processes associated with breaking waves in the surf zone are thus highly complex. In this study, LDA measurements are made with nominally regular periodic waves in a small laboratory wave flume in order to determine repetitive coherent structures in a vertical plane. LDA measures velocity at a point but the regular wave motion will enable the phase-averaged spatial picture to be approximated, with coherent structures averaged over many cycles. Phase- or ensemble-averaged (and period-averaged) kinematics may thus be obtained and dynamic pressures derived, importantly above trough level. Because the larger-scale structures are not perfectly repetitive, the moving-average method of Nadaoka *et al.* (1989) is used. The kinematics are thus split into: those due to periodic components due to wave motion (including high-order components and reflections) combined with repetitive coherent vortical structures; and those due to residual random or turbulent components. These components are interpreted further through their individual spectra and it will not be possible here to separate ensemble-averaged irrotational wave components from those due to coherent vortical structures. A method for separating out wave components from turbulence (possibly including coherent structures) has

been devised by Trowbridge & Elgar (2001), using two probes separated by a distance much less than the wavelength and greater than the turbulence length scale. This is particularly useful in the field where waves are not artificially periodic and the orientation of a probe and the wave principal axes is not always precise. Such a method could also be useful in the laboratory to separate wave motion from coherent structures, and possibly coherent structures from random turbulence, provided the length scales are sufficiently different, requiring a second LDA.

It is valuable to know the relative instantaneous magnitudes of the different terms in the RANS equations to provide physical insight and inform modelling, but they are difficult to visualize and interpret in a two-dimensional vertical plane. This is simpler through the depth-integrated terms of the RANS equations (although this will be seen to be complicated enough), and these terms are derived and evaluated from the kinematics data. The air/water interface is in reality a turbulent aerated two-phase flow, as analysed in Brocchini & Peregrine (2001), which is beyond the scope of the present measurements. In determining these terms, a discontinuous air/water interface is assumed, as in irrotational waves, which will be justified *a posteriori* if the terms in the equations balance. These terms naturally relate to the terms in the depth-averaged shallow-water equations, which are solved here, following the method of Stansby (2003) for solitary waves. This has also recently been applied to the overtopping of a sloping sea wall (Stansby & Feng 2004), giving reasonable predictions.

Such experimental measurements and analysis are very time consuming and only one case is presented. While it is known that the characteristics of breaking waves are highly dependent on their defining parameters, e.g. the surf similarity parameter, the results will provide a general qualitative assessment of coherent flow structures and the different flow properties. Their quantitative evaluation for one case will also be useful for assessing more complete flow models, of the kind mentioned above.

2. Experiment and data analysis

The intention was to generate substantial breaking waves in a laboratory flume and measure detailed kinematics using LDA. A relatively compact region enclosed in a box is desirable to satisfy safety requirements. Temporal point velocity measurements were thus made and regular waves of slowly varying form (on a small slope) enable temporal variations to be approximately transformed to spatial through $\partial/\partial t = -c\partial/\partial x$, where t is time, x is the horizontal coordinate and c is the local slowly-varying wave speed which may be obtained from surface-elevation measurements. This strictly requires waves of permanent form and its use may only be justified from analysis of experimental data. An inclined beach of slope 1:20 was set up in a wave flume which was 11 m long, 0.3 m wide and 0.45 m deep. The sidewalls and the beach plate were made of Perspex to enable the use of LDA. The toe of the beach was 1.9 m from the piston wavemaker with an almost sinusoidal motion. A sketch is shown in figure 1. Regular waves with period of 2.42 s were generated in a water depth of 0.34 m at the wavemaker producing a wave height of 0.105 m at the toe of the beach. The waves broke initially at about 4.95 m from the wave paddle with an observed variation of ± 0.02 m and the ratio of wave height to still water depth was about 0.90. The variations of wave height and mean surface elevation with distance from the paddle are shown in figure 2. These conditions correspond to a surf similarity parameter $S/\sqrt{H_b/L_0} = 0.36$, where S is the beach slope and H_b and L_0 are the wave height at breaking and the deep-water wavelength. This value is close to the boundary of 0.4 between spilling and plunging breakers (Battjes 1974) although the breakers here

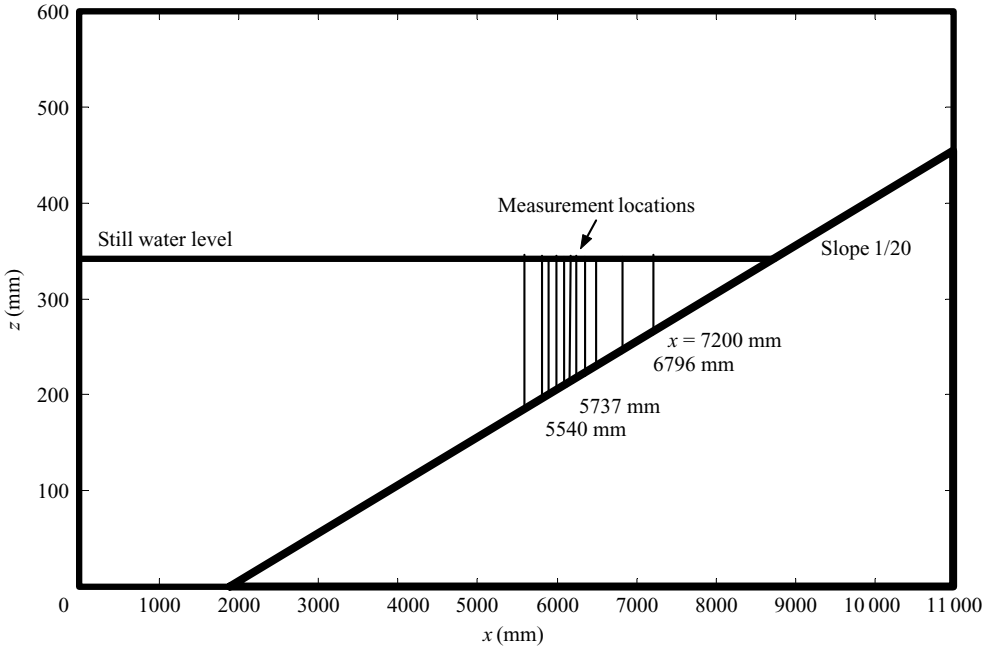

FIGURE 1. Sketch of wave flume geometry and measurement positions.

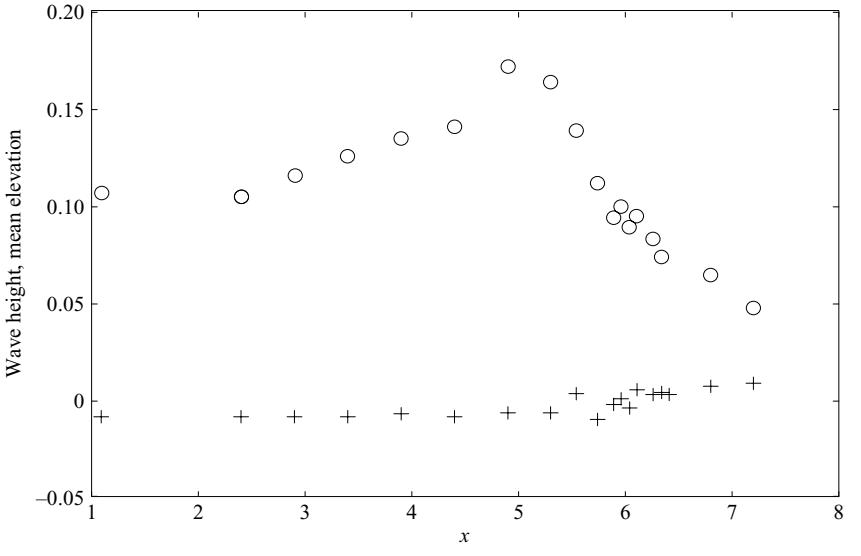

FIGURE 2. Variation of ○, wave height and +, mean elevation (m), with distance x (m), from the wavemaker.

appear visually to be weakly plunging. The set-up above the initial break point was about 10 % of the wave height there and is typical of results of experiments presented in Madsen *et al.* (1997).

Vertical LDA traverses measuring horizontal and vertical components of velocity simultaneously were made at 12 longitudinal locations at a distance x from the wavemaker (at mid position), together with surface elevation measurement. The

x (m)	5.540	5.737	5.887	5.962	6.037	6.112	6.187	6.262	6.337	6.412	6.796	7.200
c (m s)$^{-1}$	1.33	1.44	1.45	1.43	1.41	1.38	1.35	1.32	1.29	1.27	1.22	1.13
$c/\sqrt{gd}$	1.06	1.19	1.23	1.23	1.24	1.23	1.21	1.21	1.20	1.20	1.26	1.32

TABLE 1. Values of x, c and $c/\sqrt{gd}$ at 12 locations.

distance x and the wave speed c measured at these locations are given in table 1, together with the ratio $c/\sqrt{gd}$, where d is the still water depth and g is the acceleration due to gravity. These locations cover weakly plunging breakers in the outer surf zone to bores propagating in the inner surf zone and detailed results for $x = 5.540$ m and 5.737 m (plunging) and for $x = 6.796$ m and 7.200 m (bores) are presented first. The values of $c/\sqrt{gd}$ are quite close to those found by Stive (1984) for spilling breakers. The laser beams were focused at a point 30 mm (1/10th of the width of the flume) from the sidewall, giving a signal blockage (dropout) due to air bubbles of less than 15 % which was considered acceptable. The blockage naturally becomes greater as this distance is increased. Integral turbulence length scales have been estimated to vary from 0.04 to 0.18 of the water depth from the outer to the inner surf zone (Cox, Kobayashi & Okayasu 1994) and 30 mm is somewhat greater than this. Turbulence at this distance from the wall is thus not expected to be inhibited significantly by the presence of the wall. The lowest vertical measurement position was 10 mm from the bed and the highest 2.2 mm beneath a wave crest. In addition, surface elevation was measured independently at values of x shown below:

x(m)	1.094	2.404	3.404	3.904	4.404	4.904	5.304	5.598	6.104	6.604	7.104	7.604

The off-axis type LDA system (TSI product) consists of the following elements: a 4 W argon-ion laser source, a traverse table, ColourLink with signal processor (FA650 auto-correlator), DataLink and the multi-channel A/D converter. By running the Windows version FIND programme (FFW14), velocity and surface elevation can be measured simultaneously in a controlled manner with a coincident sampling rate of 300–400 Hz. For each location, 375 wave cycles were measured to ensure sufficient data have been obtained for turbulence analysis, following Nezu & Nakagawa (1993).

Conventional phase-averaging is limited in this context as each cycle of surface elevation and velocity is not exactly repetitive owing to fluctuations at the order of the wave frequency (and possibly higher) about the overall mean periodic variation, which are in addition to relatively small-scale high-frequency effects due to coherent structures and turbulence which are of interest here. In order to reduce contamination by these lower-frequency effects, the moving-average method was used by Nadaoka *et al.* (1989), where each cycle is divided into segments or blocks of time and the average velocity (and surface elevation) for each block is obtained. The average for each corresponding block over all cycles is then taken to give the overall mean cyclic variation; this will be referred to as ensemble-averaging to distinguish it from direct phase-averaging. Random residual turbulent properties are also obtained by subtracting the 'raw' velocity variation from the average for each block in each cycle, before averaging the resulting quantities over all cycles to give the overall mean cyclic variation. The decision on the number of blocks is determined by what one wants to measure. The large-scale ensemble-averaged motions and repetitive coherent vortical structures are the main emphasis of this study. The number of blocks should thus be large enough to define these structures. It was found that there was little difference in ensemble-averaged results with 120 blocks (6 samples/block at sample rate of 300 Hz)

or 240 blocks, but differences were noticeable with 60 blocks. 120 blocks thus appear to resolve the coherent structures with residual superimposed random turbulence above the Nyquist frequency of 60 × wave frequency. Further interpretation may be obtained from the velocity spectra, some examples of which are shown in figure 3 for $x = 5.54$ m and 7.2 m, before application of the moving-average method. Gradients of approximately $-5/3$ (on the log/log scale), typical of isotropic (inertia-range) turbulence, and -3, typical of two-dimensional frozen turbulence (e.g. Lesieur 1990), are seen on the graphs. The gradients of $-5/3$, occur sometimes down to a frequency of 1 Hz. A background gradient close to -3 only appears to occur with $x = 5.54$ m at mid depth (also near the bed, not shown) where there are marked harmonics at frequencies between about 2 and 7 Hz. This does not occur at still water level or at $x = 7.2$ m at any depth. The Nyquist filter frequency is about 25 Hz and it is clear that random turbulence below this frequency is lost in the moving-average process. The turbulence quantities thus obtained will only be superimposed residual values of relatively high frequency, and not representative of all turbulence energy. In spite of the approximately $-5/3$ gradients, it will be seen from the Reynolds stresses below that this residual turbulence is far from isotropic.

Plots of ensemble-averaged velocity vectors are shown in figure 4 for weakly plunging breakers and propagating bores. Note that the plots are against $T - t$ (not t), where t is time and T is wave period, which is (approximately) proportional to the horizontal coordinate. The velocity magnitudes in the roller (away from the immediate vicinity of the toe) are similar to the phase speed, with maxima up to 20 % higher initially and up to 20 % lower in the bores. Higher values with initial plunging are to be expected as crests overturn and lower values in bores are presumably due to the diffuse nature of the rollers, discussed further below. The maximum horizontal velocity occurs just above the toe initially, with magnitudes relative to the horizontal velocity at the crest of 1.21 and 1.54 at $x = 5.54$ m and 5.737 m, respectively. These are similar to values obtained by Qiao & Duncan (2001) for the initial stages of gentle spilling breakers. As a check on experimental accuracy, the horizontal volume flux over one period $\int_0^T \int_{z_b}^{\tilde{\eta}} \tilde{u}\, \mathrm{d}z\, \mathrm{d}t$, which should be zero, was evaluated for each location and normalized by $\int_0^T \int_{z_b}^{\tilde{\eta}} |\tilde{u}|\, \mathrm{d}z\, \mathrm{d}t$. In these formulae, and for vorticity below, x and z are horizontal and vertical coordinates, u and w are horizontal and vertical velocities, and the tilde denotes ensemble-averaged; η and z_b are the surface and bed elevation, respectively. Values of this flux ratio were less than 5 %, indicating an acceptable level of accuracy. Corresponding vorticity contours are shown in figure 5, where vorticity $\tilde{\omega} = \partial\tilde{u}/\partial z - \partial\tilde{w}/\partial x$. Concentrated vorticity is apparent in the roller region as multiple structures after the initiation of breaking and is spread along the free surface for bores; these are repetitive showing periodic coherent structures, bearing in mind that the results are the average of 375 cycles. The vorticity generation is shown at $x = 5.54$ m and 5.737 m, where multiple coherent vortices originate, and their further evolution is shown at $x = 5.887$ m, 5.962 m, 6.037 m and 6.187 m. The vortices are all clockwise, as sketched by Nadaoka *et al.* (1989) for spilling breakers, and spread seaward relative to the crest before inclining towards the bed at $x = 6.037$ m and forming a single large coherent region at $x = 6.187$ m. This may be considered to be the end of the plunging region and the start of bore propagation eventually resulting in the structures shown at $x = 6.796$ m and 7.2 m, with vorticity distributed along the surface. For the initial breakers at $x = 5.54$ m and 5.737 m, the maximum vorticity is about $65\ \mathrm{s}^{-1}$ at the toe of the breaker. This quickly reduces to about $35\ \mathrm{s}^{-1}$ for $x = 5.887$ m to 6.178 m which is maintained for bores at $x = 6.796$ and 7.2 m, where there is vorticity upstream of the breaker from the passage of previous breakers, as well as downstream. The drop

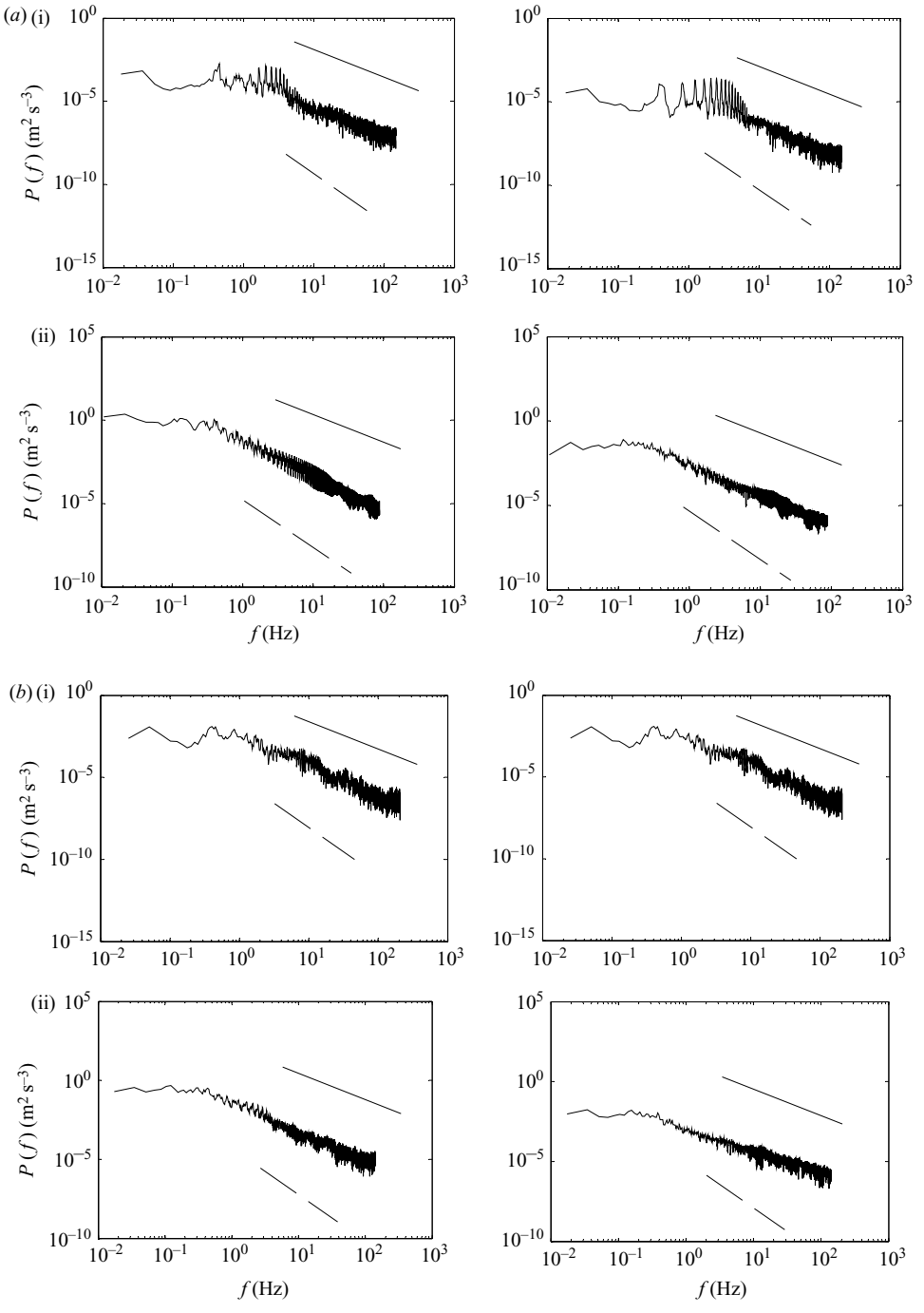

FIGURE 3. Horizontal and vertical velocity spectra (right-hand and left-hand, respectively) for initial breaking at (*a*) $x = 5.54$ m and (*b*) 7.2 m: (i) at mid depth and (ii) still surface level. The full line shows the $-5/3$ gradient and the dashed line the -3 gradient. The Nyquist filter frequency resulting from ensemble averaging is 25 Hz.

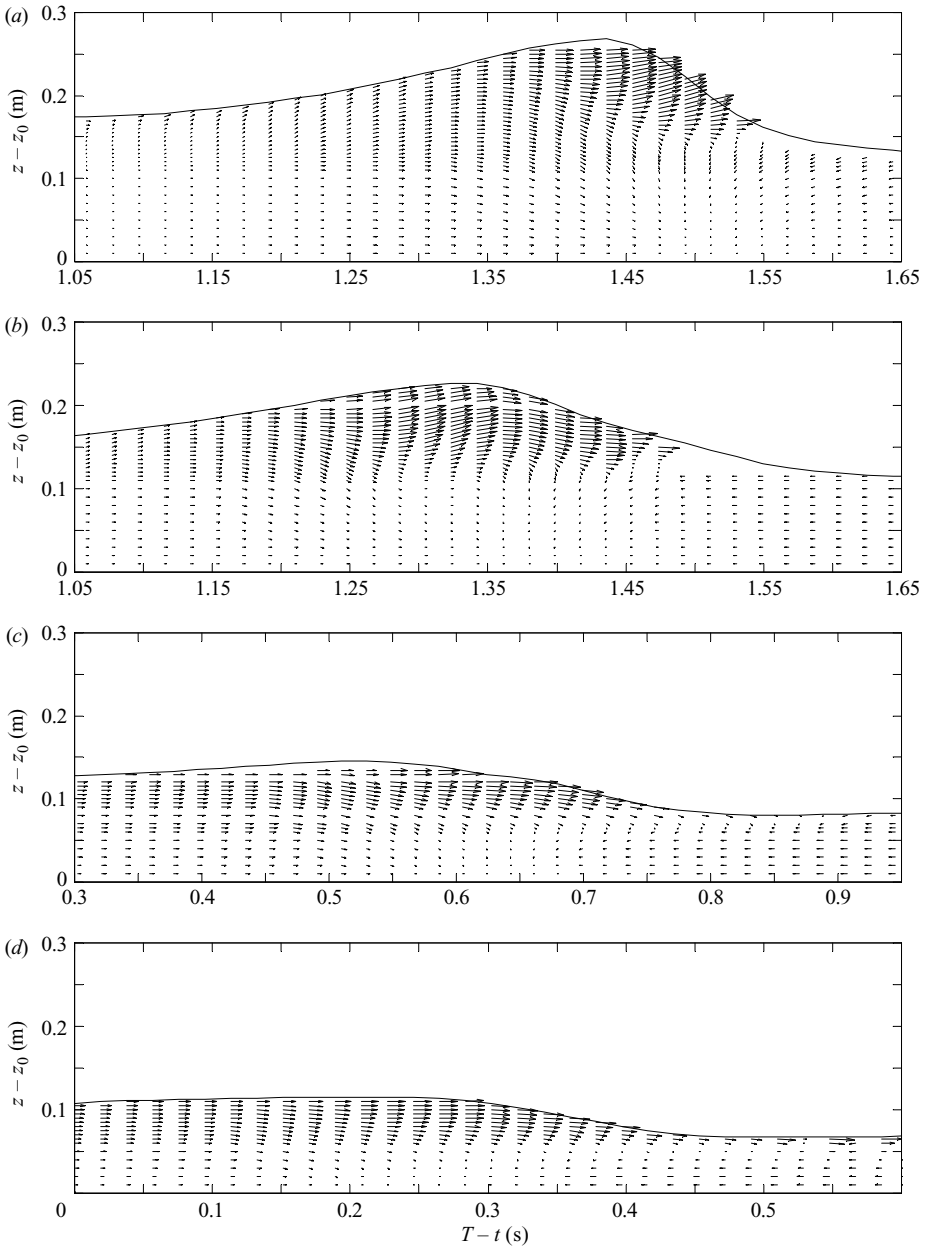

FIGURE 4. Velocity vector plots for initial breaking at (*a*) $x = 5.54$ and (*b*) 5.737 m and bores at (*c*) $x = 6.796$ and (*d*) 7.2 m.

in maximum vorticity appears to occur where the coherent vortices spread markedly along the surface. The maximum vorticity near the toe of gentle spilling breakers was measured by Qiao & Duncan (2001) just after breaking when they found values of $|\omega|_{max} l_s/c$ of 0.2–0.9, where l_s is the surface tension length scale of about 2.7 mm. This compares with a value of 0.125 for the initial stages here, suggesting that this is not the relevant length scale for these breakers which appear weakly plunging. The maximum vorticity and other values for $x = 5.54$, 5.737, 6.796 and 7.2 m are tabulated in table 2.

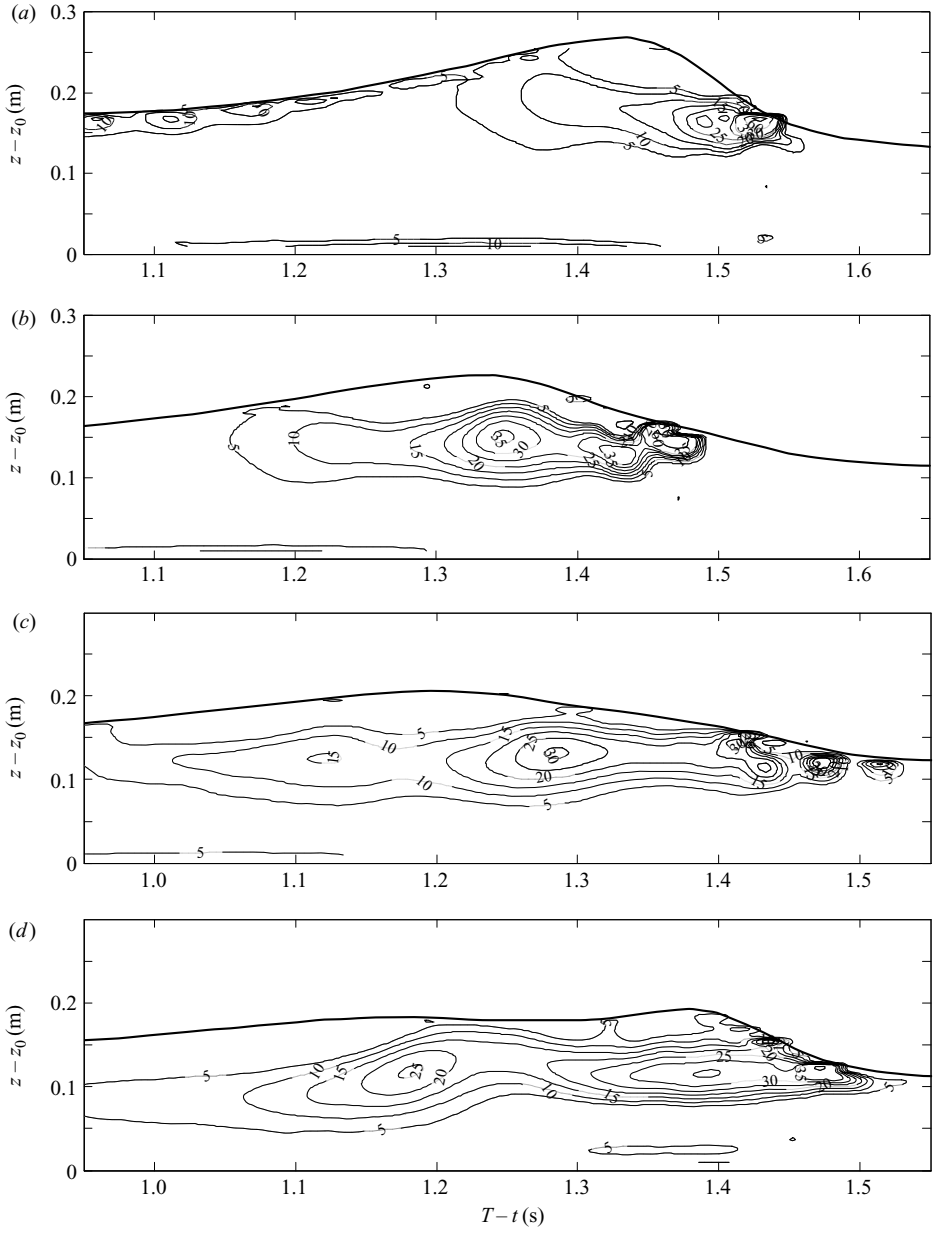

FIGURE 5(*a–d*). For caption see facing page.

Period-averaged velocity vectors and vorticity are shown in figure 6. The onshore velocity above trough level and the undertow below are clearly visible across the surf zone. An upwards velocity region around $x = 6.2$ m is also visible (although note the distorted scale) and this appears to be the end of the region with the formation of multiple coherent vortices (shown in figure 5). The period-averaged vorticity field is as expected with a thick layer of clockwise vorticity around the trough line and counterclockwise vorticity near the bed. It is perhaps surprising that the end of the initial region, as described above, is marked by regions of concentrated mean

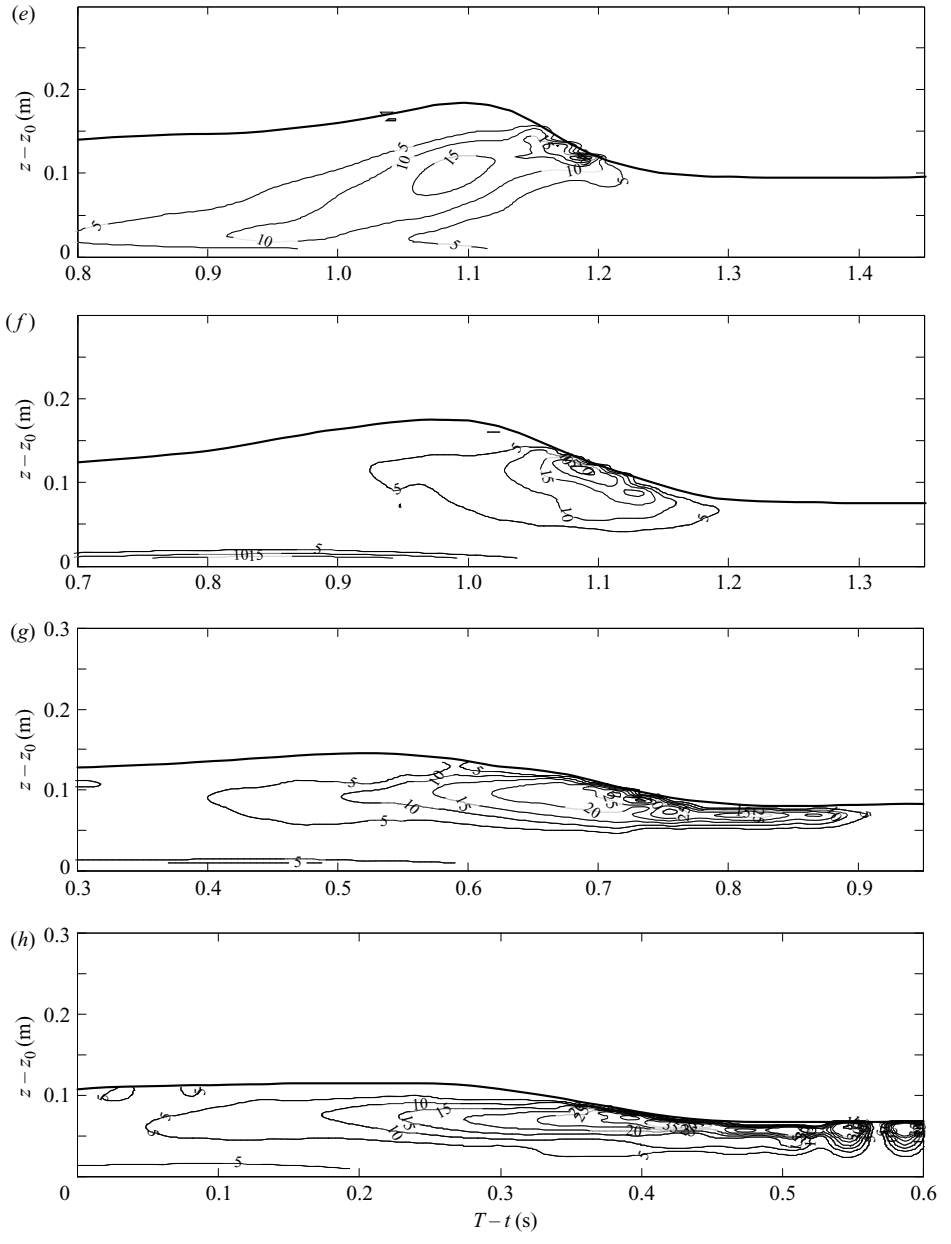

FIGURE 5. Vorticity, $\widetilde{\omega}$, (s^{-1}) contour plots for initial breaking at (*a*) $x = 5.54$, (*b*) 5.737, (*c*) 5.887, (*d*) 5.962, (*e*) 6.037 and (*f*) 6.187 m and bores at (*g*) $x = 6.796$ and (*h*) 7.200 m. Clockwise rotation is positive.

clockwise vorticity. It is also interesting to see the velocity vector field averaged over the 'wet' period (the time for which a point is immersed in a cycle) and normalized by the wave speed, as measured at a given location. This is shown in figure 7 and reflects the comments made about figure 4. The maximum values occur at the crest. During the initiation of breaking, maximum values are just greater than unity and in the bore region just less than unity. Magnitudes decrease to small values at and below trough level, as the wet period becomes equal to the wave period.

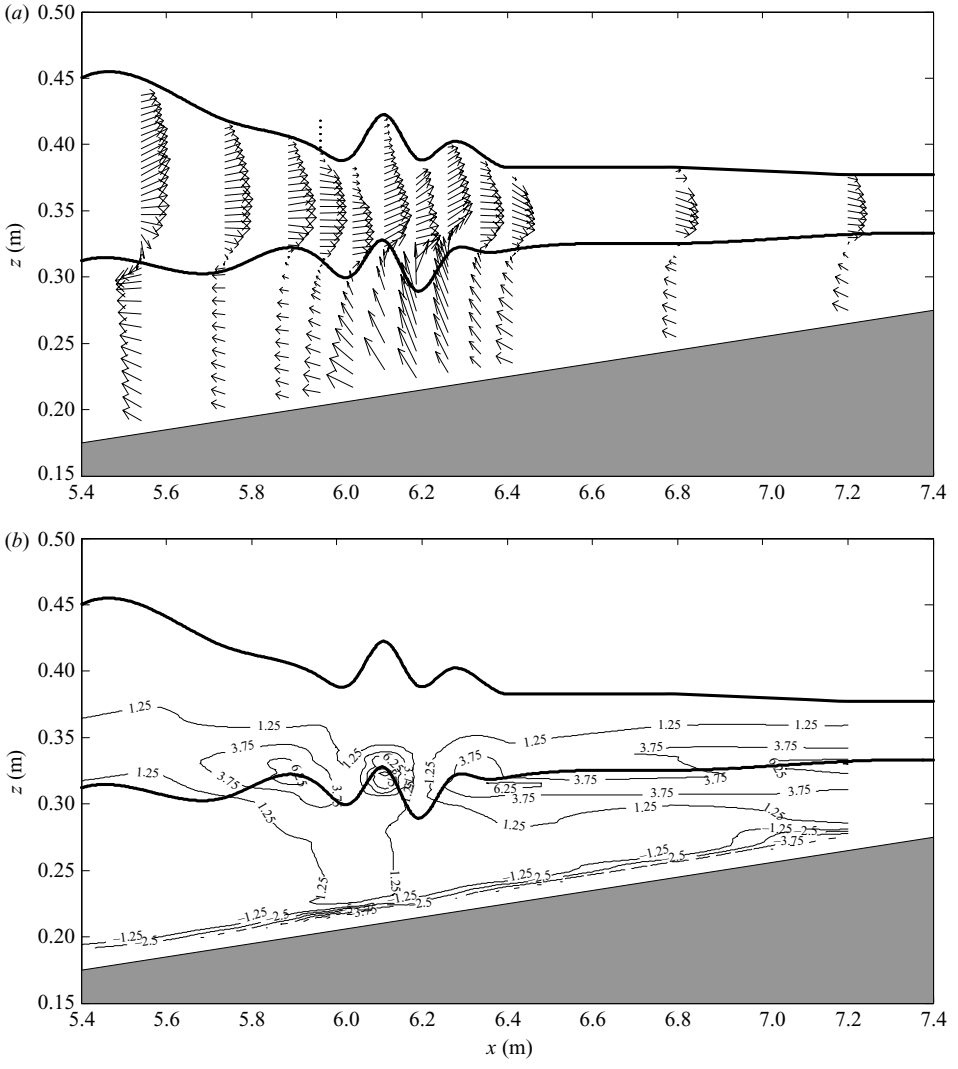

FIGURE 6. Period-averaged (*a*) velocity vectors and (*b*) vorticity. The full lines show the crest and trough trajectories.

Ensemble-averaged dynamic pressure, $\widetilde{p_D}$, (pressure minus its hydrostatic component) contours are shown in figure 8. The way in which dynamic pressure is calculated from kinematics is defined in § 4. For the initial weakly plunging breakers, very low dynamic pressures are created in the roller region with minimum values of $\widetilde{p_D}/\rho g H$ of –0.4, where ρ is water density and H is wave height, at $x = 5.54$ m reducing to –0.21 at $x = 6.112$ m. For $x > 6.187$ m, after the end of the initial region, negative dynamic pressures have reduced markedly, being negligible by $x = 6.337$ m (not shown). Dynamic pressure at the surface is of course zero, and is negative at the bed shoreward of the breaker and positive seaward with similar maximum magnitudes. The maximum magnitude of $\widetilde{p_D}/\rho g H$ is approximately 0.2 at $x = 5.54$ m and 0.13 at $x = 7.2$ m. Dynamic pressure magnitudes are thus greater during initial breaking than in bores but remain significant for bores, as will also be shown below for depth-integrated quantities.

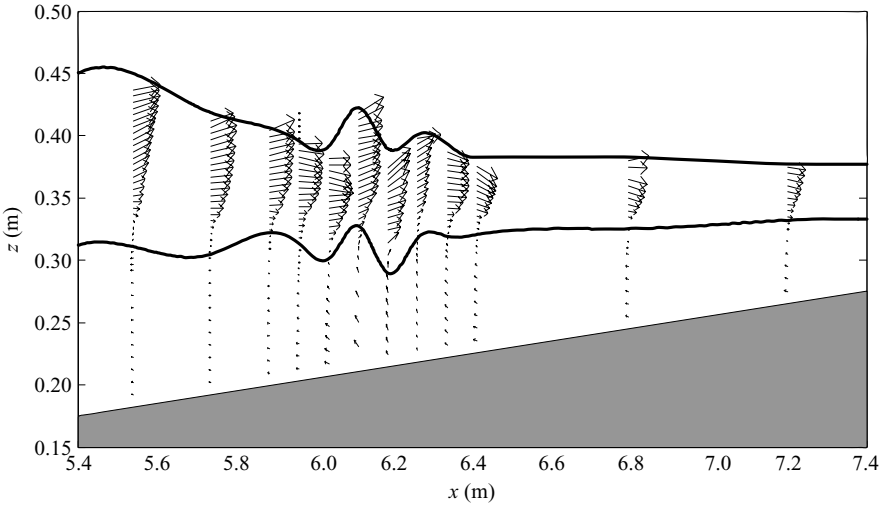

FIGURE 7. Wet period-averaged velocity vectors normalized by measured local wave celerity. The full lines show the crest and trough trajectories.

Contours of horizontal normal stress due to residual turbulence, $-\rho\widetilde{u'^2}$, are shown in figure 9, of vertical normal stress, $-\rho\widetilde{w'^2}$, in figure 10 and shear stress, $-\rho\widetilde{u'w'}$, in figure 11. The dash denotes residual turbulent component, resulting from the moving-average method with 120 blocks. Note that negative normal stress quantities are actually plotted, i.e. positive quantities, and water density $\rho = 1000\,\mathrm{kg\,m^{-3}}$. It can be seen that $\widetilde{u'^2}$ is greatest close to the crest at all positions. The contours are elliptical initially, at $x = 5.54$ m and 5.74 m, and elongated under bores, at $x = 6.80$ m and 7.20 m. Magnitudes initially, with maxima of $0.055\,\mathrm{m^2\,s^{-2}}$ and $0.045\,\mathrm{m^2\,s^{-2}}$ for $x = 5.54$ m and 5.74 m, respectively, are greater than under bores, with maxima of $0.035\,\mathrm{m^2\,s^{-2}}$ for $x = 6.976$ m and 7.2 m, respectively. On the other hand, $\widetilde{w'^2}$ is greatest at the toe of the roller initially and for bores. Although the contour patterns are again fairly elliptical initially and elongated for bores, they have a different orientation from the $\widetilde{u'^2}$ contours, relative to the wave, emphasizing the anisotropy of the turbulence. The magnitudes are less than for horizontal stress, with maxima of $0.040\,\mathrm{m^2\,s^{-2}}$ and $0.030\,\mathrm{m^2\,s^{-2}}$ for $x = 5.54$ m and 5.74 m, respectively. There are very small maxima of $0.005\,\mathrm{m^2\,s^{-2}}$ for bores at $x = 6.80$ m and 7.20 m. The term $-\widetilde{u'w'}$ in figure 11 is clearly greatest at the toe of the roller initially with maxima of $0.015\,\mathrm{m^2\,s^{-2}}$, which is markedly less than the normal stress magnitudes. This is also the case for bores with much smaller magnitudes and maxima of about $0.002\,\mathrm{m^2\,s^{-2}}$, with very small background magnitudes persisting over much of the flow region.

3. Comparison with hydraulic jumps

Some of the above results are collated in table 2 for comparison with hydraulic jump results. The upstream and downstream depths of the hydraulic jump, h_1 and h_2, are assumed to be equivalent to the minimum and maximum depths as the breaker passes and the upstream velocity, u_1, is equivalent to the sum of the wave celerity and the corresponding depth-averaged velocity which is the minimum value. Examples of variation of depth and depth-averaged velocity with time are shown in § 5. Svendsen *et al.* (2000) measured vorticity in hydraulic jumps with Froude number,

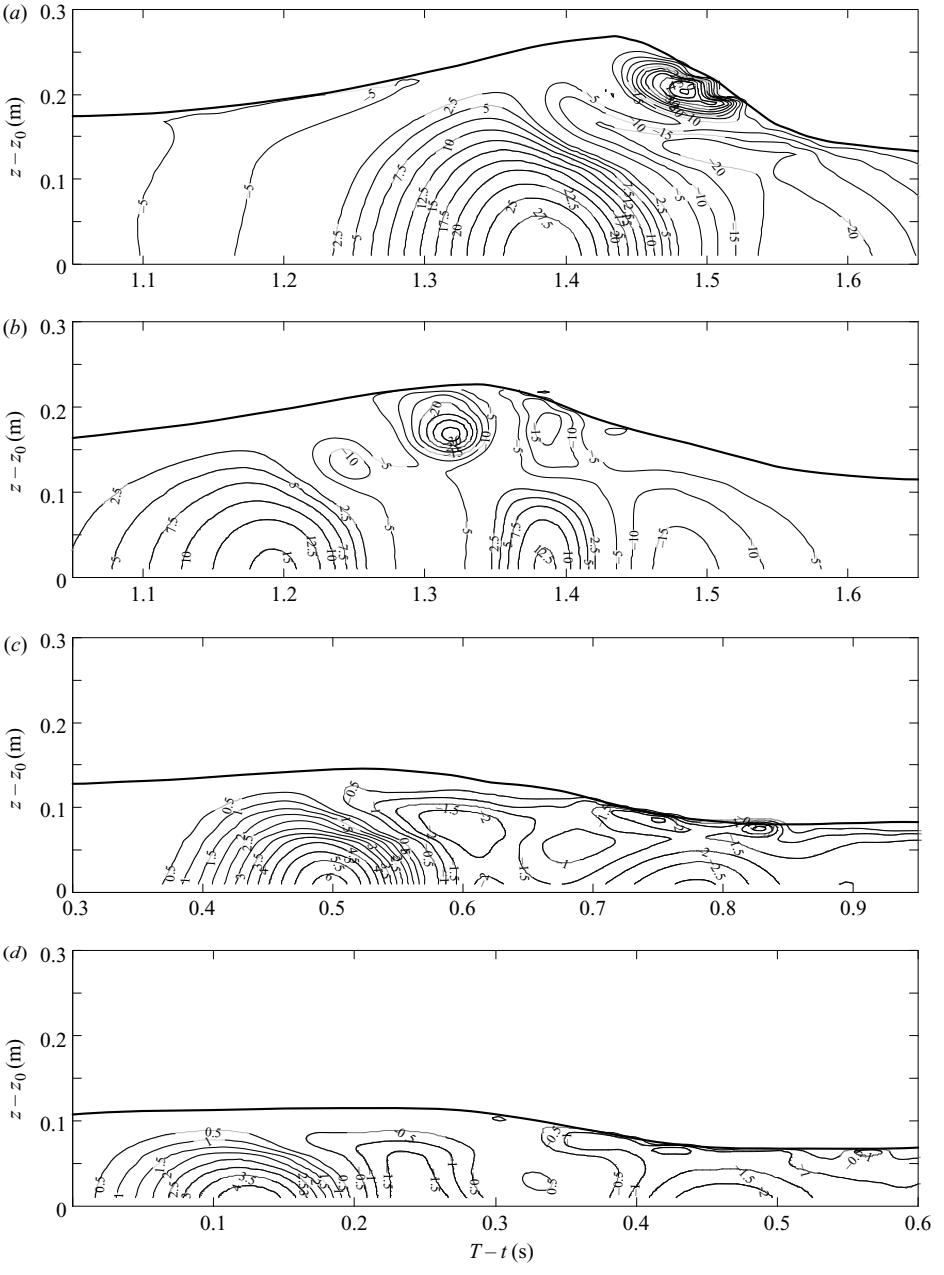

FIGURE 8. Dynamic pressure ($(\widetilde{p_D}/\rho) \times 100$), ($m^2\,s^{-2}$), contour plots for initial breaking at (*a*) $x = 5.54$ and (*b*) 5.737 m and bores at (*c*) $x = 6.796$ and (*d*) 7.200 m.

$Fr = u_1/\sqrt{g\,h_1}$, in the range 1.38 to 1.56, finding that the non-dimensional vorticity $\omega h_2 \xi / u_1$ along the base of the roller collapsed the data for the range of conditions rather well. The maximum at the toe of the roller has an extrapolated value of about 17 (Veeramony & Svendsen 2000) and may be compared with the maximum value at the toe of the breakers in these experiments. Table 2 shows that the equivalent Froude numbers are slightly higher, ranging from 1.46 to 1.76, and that the maximum

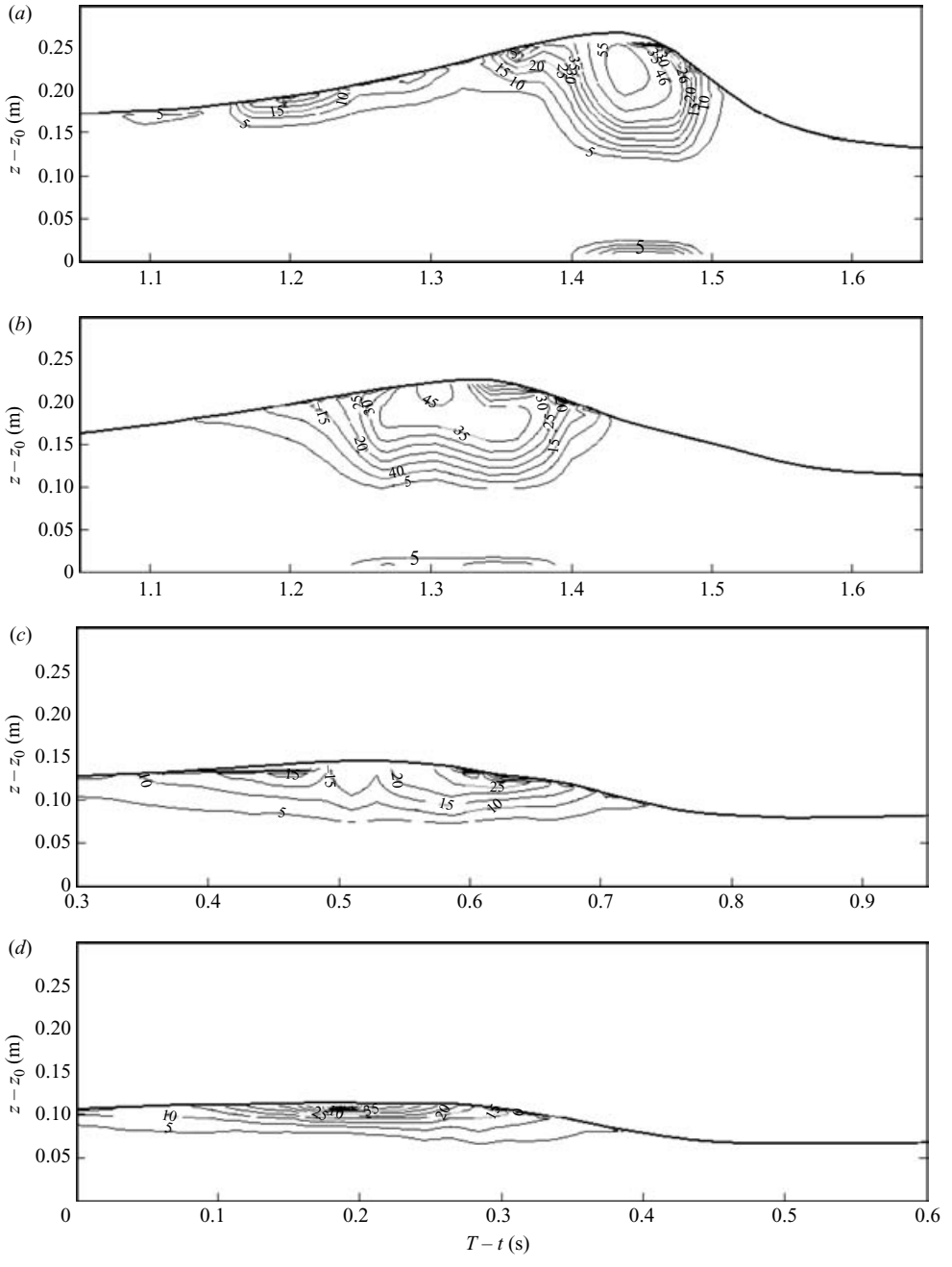

FIGURE 9. Horizontal residual turbulent normal stress ($\rho\widetilde{u'^2}$), (N m^{-2}), contour plots for initial breaking at (*a*) $x = 5.54$ and (*b*) 5.737 m and bores at (*c*) $x = 6.796$ and (*d*) 7.200 m.

non-dimensional vorticity ranges from 22.1 at the initiation of breaking to 4.5 in the bore region. A value for an albeit weakly plunging breaker somewhat larger than the hydraulic jump value is perhaps to be expected as the transitory overturning wave generates a jet which impacts below with relatively greater velocities than in the continuous mixing-layer behaviour of a hydraulic jump. The marked reduction

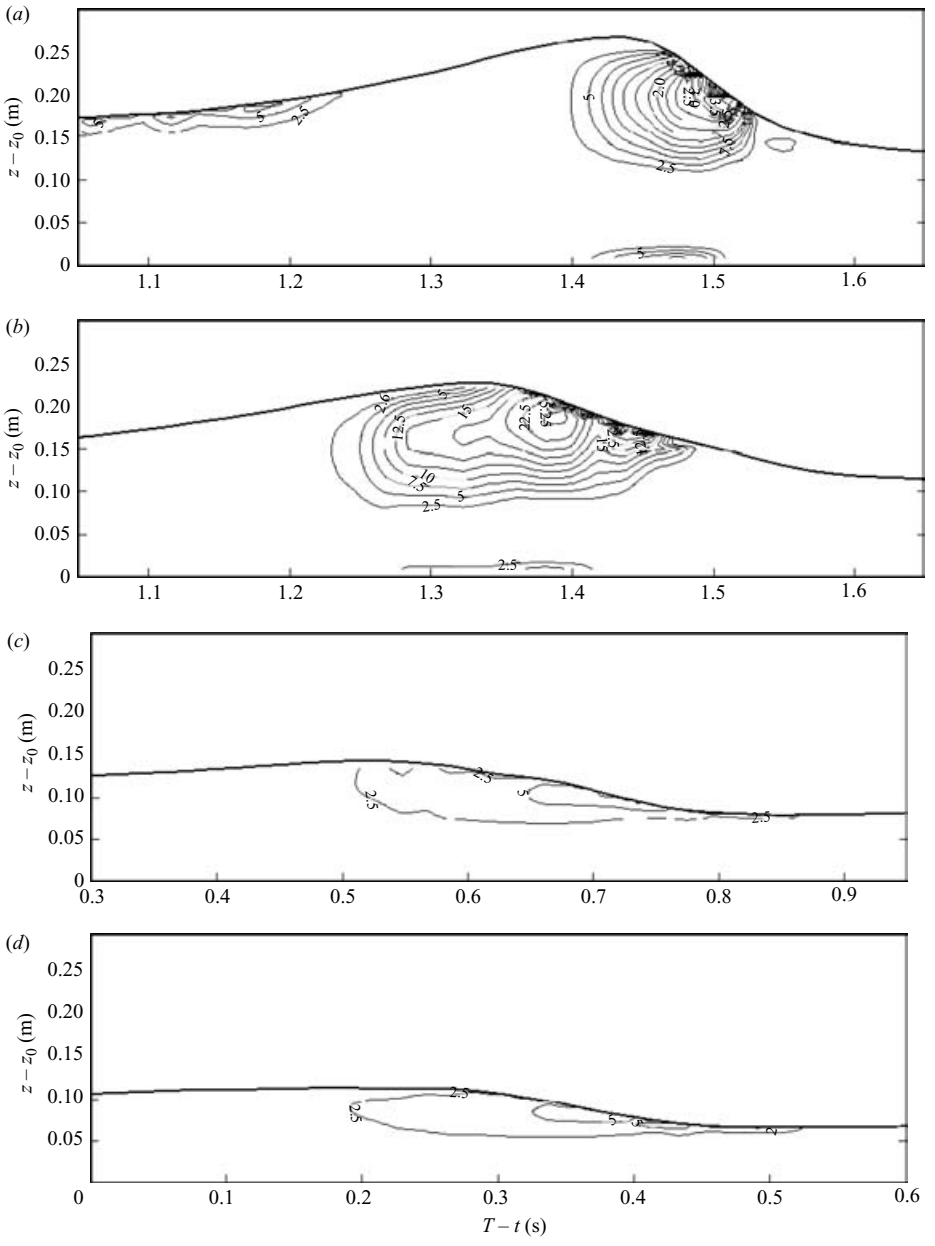

FIGURE 10. Vertical residual turbulent normal stress ($\rho\widetilde{w'^2}$), (N m^{-2}), contour plots for initial breaking at (*a*) $x = 5.54$ and (*b*) 5.737 m and bores at (*c*) $x = 6.796$ and (*d*) 7.200 m.

for the bore behaviour which follows is probably due to mixing and dissipation by turbulence resulting from continuous breaking in the surf zone; equivalent turbulence is not present in a hydraulic jump which is essentially a single stationary event.

The maxima of $\widetilde{u'^2}/u_1^2$ are 0.02, 0.015, 0.17 and 0.016 at $x = 5.54$ m, 5.74 m, 6.80 m and 7.20 m, respectively, comparing with maximum hydraulic jump values of 0.06 from Svendsen *et al.* (2000) and 0.05 from Liu, Rajaratnam & Zhu (2004). Note that

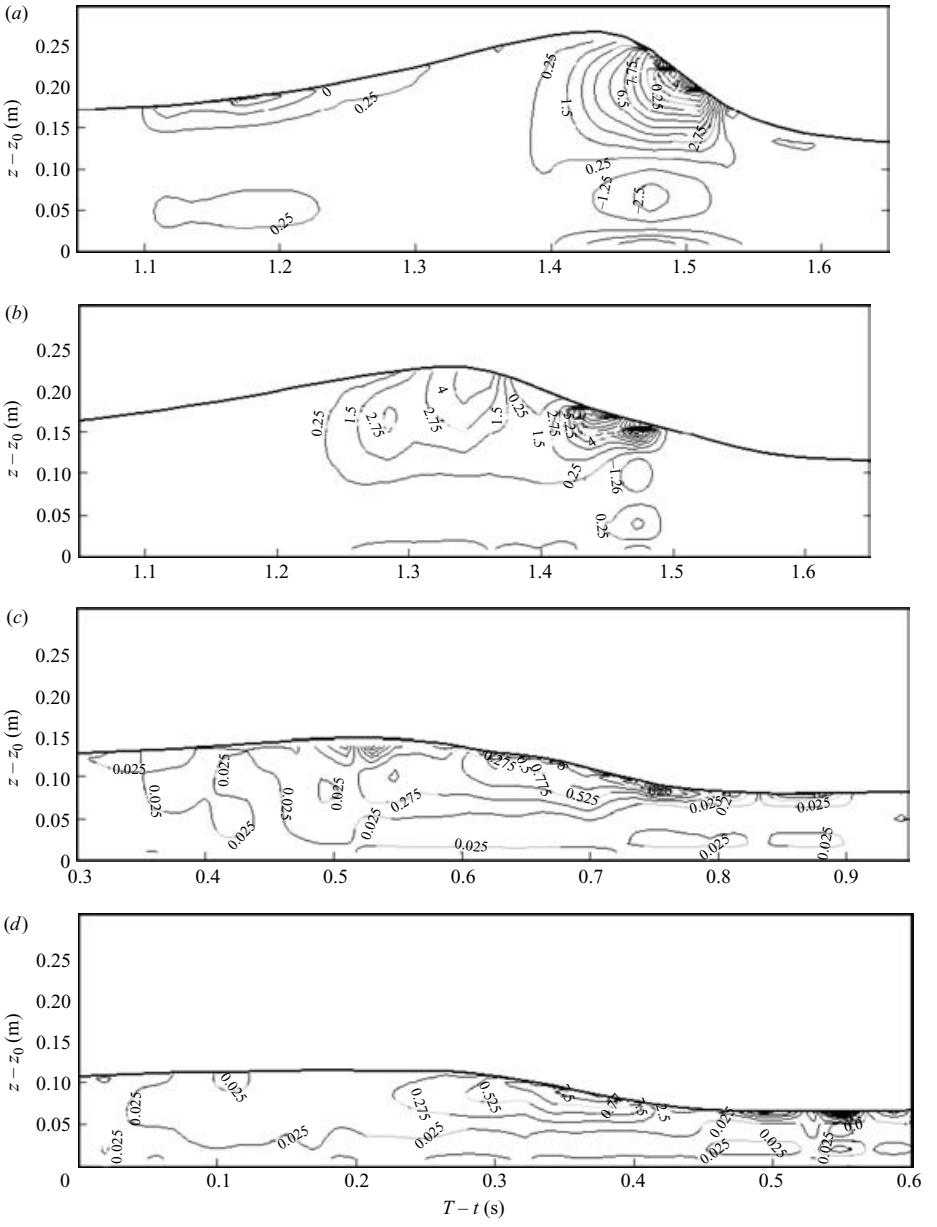

FIGURE 11. Residual turbulent shear stress $(-\rho\widetilde{u'w'})$, (N m^{-2}), contour plots for initial breaking at (*a*) $x = 5.54$ and (*b*) 5.737 m and bores at (*c*) $x = 6.796$ and (*d*) 7.200 m.

Froude numbers for Liu *et al.* (2004) were in the ranges 2.0–3.3. There are smaller maxima of $\widetilde{w'^2}/u_1^2$ of about 0.015 and 0.01 at $x = 5.54$ m and 5.74 m, and 0.002 at $x = 6.8$ m and 7.2 m. These compare with hydraulic jump values of 0.06 from Svendsen *et al.* (2000) and 0.006 from Liu *et al.* (2004). The maxima of $-\widetilde{u'w'}/u_1^2$ are 0.0085 and 0.005 at $x = 5.54$ m and 5.74 m and 0.001 at $x = 6.8$ m and 7.2 m, with very small background magnitudes persisting over much of the flow region for the latter. For the hydraulic jump experiments of Svendsen *et al.* (2000), the maximum $-\widetilde{u'w'}/u_1^2$ was between 0.02 and 0.03, while for those of Liu *et al.* (2004) it was about 0.008.

x (m)	5.54	5.74	6.80	7.20
c (m s^{-1})	1.33	1.44	1.22	1.13
u_1(m s^{-1})	1.65	1.74	1.45	1.46
h_1(m)	0.13	0.12	0.08	0.070
h_2(m)	0.27	0.23	0.145	0.115
$\xi = h_2/h_1$	2.08	1.92	1.81	1.64
$Fr = u_1/\sqrt{g\,h_1}$	1.46	1.60	1.64	1.76
ω_s(s^{-1}) at toe	65	65	35	35
$\omega_s\, h_2\xi/u_1$	22.1	16.5	6.35	4.5
$\widetilde{u'^2}$(m^2 s^{-2})	0.055	0.045	0.035	0.035
$\widetilde{u'^2}/u_1^2$	0.020	0.015	0.017	0.016
$\widetilde{w'^2}$(m^2 s^{-2})	0.04	0.03	0.005	0.005
$\widetilde{w'^2}/u_1^2$	0.015	0.010	0.002	0.002
$-\widetilde{u'w'}$(m^2 s^{-2})	0.015	0.015	0.002	0.002
$-\widetilde{u'w'}/u_1^2$	0.0085	0.005	0.001	0.001

TABLE 2. Surf zone vorticity and turbulence characteristics.

The turbulence stresses obtained for these experiments are generally markedly less than for the hydraulic jump experiments and this is mainly due to the method of analysis. In this study, residual 'random' turbulence is differentiated from coherent structures and some turbulence is obscured in the moving-average process. In hydraulic jumps, all unsteady motion, including coherent structures, is classed as turbulence and the present analysis applied to hydraulic jumps would thus give smaller values. However, there are also differences between the experiments of Svendsen *et al.* (2000) and Liu *et al.* (2004), albeit for somewhat different Froude numbers, notably for vertical normal stress and shear stress. There are further quite marked differences from earlier authors quoted in Liu *et al.* (2004). There are also qualitative differences in the distribution of stresses between these experiments and hydraulic jumps. The maximum stresses in hydraulic jumps always occur at the toe of the roller and this is the case here for $\widetilde{w'^2}$ and $-\widetilde{u'w'}$, but not for $\widetilde{u'^2}$ where the maxima occur near the crest. For these experiments $\widetilde{u'^2}/u_1^2$ decreases slightly from the initiation of breaking to bores while $\widetilde{w'^2}/u_1^2$ and $-\widetilde{u'w'}/u_1^2$ decrease markedly.

4. RANS depth-integrated shallow-water equations

For this analysis, we assume that the flow is strictly periodic. In a two-dimensional vertical (2DV) plane, horizontal and vertical velocities (u, w) at a point have phase-averaged components $(\tilde{u}, \tilde{w})$ and turbulent components (u', w')

$$\left.\begin{aligned} u &= \tilde{u} + u', \\ w &= \tilde{w} + w'. \end{aligned}\right\} \tag{1}$$

Phase-averaging (taking the periodic mean) gives, for continuity,

$$\frac{\partial \tilde{u}}{\partial x} + \frac{\partial \tilde{w}}{\partial z} = 0, \tag{2}$$

and for horizontal momentum

$$\frac{\partial \tilde{u}}{\partial t} + \frac{\partial(\tilde{u}^2)}{\partial x} + \frac{\partial(\tilde{u}\tilde{w})}{\partial z} = -\frac{1}{\rho}\frac{\partial \tilde{p}}{\partial x} - \frac{\partial(\widetilde{u'^2})}{\partial x} - \frac{\partial(\widetilde{u'w'})}{\partial z}, \tag{3}$$

where pressure $p = \tilde{p} + p'$. Simplistically assuming a single-phase flow, the kinematic free-surface boundary condition for water surface elevation, $\eta = \tilde{\eta} + \eta'$, is given by

$$\left.\begin{aligned} w_s &= \frac{\partial \eta}{\partial t} + u_s \frac{\partial \eta}{\partial x}, \\ \tilde{w}_s + w' &= \frac{\partial(\tilde{\eta} + \eta')}{\partial t} + (\tilde{u}_s + u')\frac{\partial(\tilde{\eta} + \eta')}{\partial x}, \end{aligned}\right\} \tag{4}$$

where s denotes surface values and b, below, bed values. Phase-averaging gives

$$\tilde{w}_s = \frac{\partial \tilde{\eta}}{\partial t} + \tilde{u}_s \frac{\partial \tilde{\eta}}{\partial x} + \widetilde{u' \frac{\partial \eta'}{\partial x}}. \tag{5}$$

The last term is difficult to evaluate experimentally. It has also been stated above that terms associated with the turbulent aerated two-phase flow at the air/water interface, e.g. Brocchini & Peregrine (2001), are to be ignored. This is justified below, at least in an instantaneous depth-integrated sense, where it is shown that depth-integrated horizontal force/momentum flux terms balance closely. Such surface assumptions have also been made in relation to depth-integrated force/momentum flux terms in hydraulic jumps by Svendsen *et al.* (2000). Integrating over depth, from the bed to the water surface, $\int_{z_b}^{\tilde{\eta}} \ldots \mathrm{d}z$, for example $\bar{\tilde{u}}\,\tilde{h} = \int_{z_b}^{\tilde{\eta}} \tilde{u}\,\mathrm{d}z$, where h is water depth and the overbar indicates depth average, applying the Leibnitz theorem and the phase-averaged kinematic free-surface (and bed) boundary condition, gives, for continuity,

$$\frac{\partial \tilde{\eta}}{\partial t} + \frac{\partial(\tilde{h}\bar{\tilde{u}})}{\partial x} = 0, \tag{6}$$

and for horizontal momentum with pressure defined by its hydrostatic and dynamic components, $\tilde{p} = \rho g(\tilde{\eta} - z) + \tilde{p}_D$,

$$\frac{\partial\left(\int_{z_b}^{\tilde{\eta}} \tilde{u}\,\mathrm{d}z\right)}{\partial t} + \frac{\partial\left(\int_{z_b}^{\tilde{\eta}} \tilde{u}^2\,\mathrm{d}z\right)}{\partial x} = -g\tilde{h}\frac{\partial \tilde{\eta}}{\partial x} - \frac{1}{\rho}\int_{z_b}^{\tilde{\eta}} \frac{\partial \tilde{p}_D}{\partial x}\,\mathrm{d}z - \widetilde{u'w'_s} + \widetilde{u'w'_b} - \int_{z_b}^{\tilde{\eta}} \frac{\partial \widetilde{u'^2}}{\partial x}\,\mathrm{d}z. \tag{7}$$

Applying the Leibnitz theorem to the last term gives

$$-\int_{z_b}^{\tilde{\eta}} \frac{\partial \widetilde{u'^2}}{\partial x}\,\mathrm{d}z = -\frac{\partial\left(\int_{z_b}^{\tilde{\eta}} \widetilde{u'^2}\,\mathrm{d}z\right)}{\partial x} + \widetilde{u'^2}_s \frac{\partial \tilde{\eta}}{\partial x} - \widetilde{u'^2}_b \frac{\mathrm{d}z_b}{\mathrm{d}x}. \tag{8}$$

Putting $\tilde{u} = \bar{\tilde{u}} + (\tilde{u} - \bar{\tilde{u}})$, assuming u'at the bed is zero, gives

$$\underset{\text{I}}{\frac{\partial(\bar{\tilde{u}}\tilde{h})}{\partial t}} + \underset{\text{II}}{\frac{\partial(\bar{\tilde{u}}^2\tilde{h})}{\partial x}} + \underset{\text{III}}{g\tilde{h}\frac{\partial \tilde{\eta}}{\partial x}} = \underset{\text{IV}}{-\frac{1}{\rho}\int_{z_b}^{\tilde{\eta}} \frac{\partial \tilde{p}_D}{\partial x}\,\mathrm{d}z} \underset{\text{V}}{- \frac{\partial\left(\int_{z_b}^{\eta} (\tilde{u} - \bar{\tilde{u}})^2\,\mathrm{d}z\right)}{\partial x}}$$

$$\underset{\text{VI}}{-\widetilde{u'w'_s}} + \underset{\text{VII}}{\widetilde{u'w'_b}} \underset{\text{VIII}}{- \frac{\partial\left(\int_{z_b}^{\tilde{\eta}} \widetilde{u'^2}\,\mathrm{d}z\right)}{\partial x}} + \underset{\text{IX}}{\widetilde{u'^2}_s \frac{\partial \tilde{\eta}}{\partial x}}, \tag{9}$$

where the roman numerals are used to indicate the different terms. Term I is the inertia term due to (Eulerian) flow acceleration, II is the advection term and III is

the hydrostatic pressure gradient term. The dynamic pressure gradient term IV has yet to be derived. Term V is due to the vertical variation of velocity, called vertical dispersion to distinguish it from frequency dispersion. The surface and bed shear stress terms are VI and VII, respectively. The normal turbulent stress terms (VIII and IX) are not usually included, but should be evaluated. In (6) and (9), terms in $\partial/\partial x$ will be transformed to $-(1/c)(\partial/\partial t)$ in order to be evaluated from the experimental data. The justification of this transformation for slowly varying waves will be made *a posteriori* by showing that the terms in (9), evaluated from experimental data, balance relatively closely.

The dynamic pressure term may be determined from the RANS vertical momentum equation

$$\frac{\partial \tilde{w}}{\partial t} + \frac{\partial(\tilde{u}\tilde{w})}{\partial x} + \frac{\partial(\tilde{w}^2)}{\partial z} = -\frac{1}{\rho}\frac{\partial \tilde{p}_D}{\partial z} - \frac{\partial(\widetilde{u'w'})}{\partial x} - \frac{\partial(\widetilde{w'^2})}{\partial z}, \tag{10}$$

giving

$$-\left[\frac{\tilde{p}_D}{\rho}\right]_z^{\tilde{\eta}} = \int_z^{\tilde{\eta}} \frac{\partial \tilde{w}}{\partial t}\,\mathrm{d}z + \int_z^{\tilde{\eta}} \frac{\partial(\tilde{u}\tilde{w})}{\partial x}\,\mathrm{d}z + [\tilde{w}^2]_z^s + \int_z^{\tilde{\eta}} \frac{\partial(\widetilde{u'w'})}{\partial x}\,\mathrm{d}z + [\widetilde{w'^2}]_z^s. \tag{11}$$

If the surface pressure is zero, applying the Leibnitz theorem and the kinematic free surface boundary condition, gives

$$\left.\frac{\tilde{p}_D}{\rho}\right|_z = \frac{\partial}{\partial t}\int_z^{\tilde{\eta}} \tilde{w}\,\mathrm{d}z + \frac{\partial}{\partial x}\int_z^{\tilde{\eta}} \tilde{u}\tilde{w}\,\mathrm{d}z - \tilde{w}^2|_z + \int_z^{\tilde{\eta}} \frac{\partial(\widetilde{u'w'})}{\partial x}\,\mathrm{d}z + [\widetilde{w'^2}]_z^s. \tag{12}$$

In hydraulic jumps, the influence of turbulence is considered negligible (Svendsen *et al.* 2000) and is almost certainly less here, owing to the different definitions of turbulence described above. At a point with vertical coordinate z

$$\frac{\tilde{p}_D}{\rho} = \frac{\partial}{\partial t}\int_z^{\tilde{\eta}} \tilde{w}\,\mathrm{d}z + \frac{\partial}{\partial x}\int_z^{\tilde{\eta}} \tilde{u}\tilde{w}\,\mathrm{d}z - \tilde{w}^2. \tag{13}$$

Using the space–time transformation gives

$$\frac{\tilde{p}_D}{\rho} = \frac{\partial}{\partial t}\int_z^{\tilde{\eta}} \tilde{w}\,\mathrm{d}z - \frac{1}{c}\frac{\partial}{\partial t}\int_z^{\tilde{\eta}} \tilde{u}\tilde{w}\,\mathrm{d}z - \tilde{w}^2. \tag{15}$$

For the depth-averaged horizontal momentum (9), we require

$$-\frac{1}{\rho}\int_{z_b}^{\tilde{\eta}} \frac{\partial \tilde{p}_D}{\partial x}\,\mathrm{d}z = -\frac{1}{\rho}\frac{\partial}{\partial x}\int_{z_b}^{\tilde{\eta}} \tilde{p}_D\,\mathrm{d}z + \frac{\tilde{p}_{Ds}}{\rho}\frac{\partial \tilde{\eta}}{\partial x} - \frac{\tilde{p}_{Db}}{\rho}\frac{\mathrm{d}z_b}{\mathrm{d}x}. \tag{16}$$

With $\tilde{p}_{Ds} = 0$ and the space–time transformation

$$-\frac{1}{\rho}\int_{z_b}^{\tilde{\eta}} \frac{\partial \tilde{p}_D}{\partial x}\,\mathrm{d}z = \frac{1}{\rho c}\frac{\partial}{\partial t}\int_{z_b}^{\tilde{\eta}} \tilde{p}_D\,\mathrm{d}z - \frac{\tilde{p}_{Db}}{\rho}\frac{\mathrm{d}z_b}{\mathrm{d}x}. \tag{17}$$

The nine terms in (9) have been evaluated from LDA measurements.

5. Depth-integrated experimental results

Although we are mainly concerned with the force/momentum equations (9), the balance of the two ensemble-averaged terms in the depth-integrated continuity, (6) is assessed first as an independent test of the space/time transformation and experimental accuracy. Examples of the two terms and the remainder are shown in figure 12

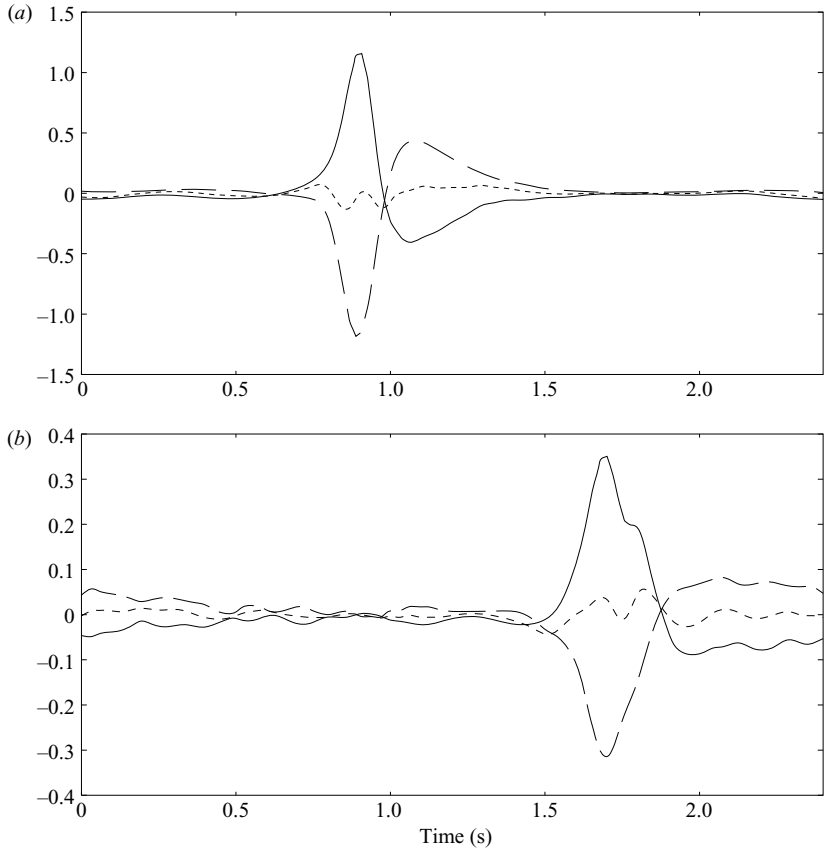

FIGURE 12. Terms in depth-integrated continuity (6) against time: $\partial\tilde{\eta}/\partial t$, full line; $(-1/c)(\partial(\tilde{h}\tilde{\bar{u}})/\partial t)$, dashed line; remainder dotted. (*a*) at $x = 5.54$ m, (*b*) at 6.80 m.

for the initial breaking region at $x = 5.54$ m and a bore at $x = 6.80$ m. The remainder term is small, but not negligible, with a maximum of about 15 % of the maximum magnitude for the bore. The relative errors in the remainder term for the force/momentum equation will be seen to be smaller and the greater errors in (6) could be due to $\partial\eta/\partial t$, as surface elevation is measured by a capacitance wave probe with an uncertain error due to the variably aerated interface which will be exaggerated by differentiation with respect to time.

The depth-integrated terms I, II, III, IV, V in (9) are plotted against time in figures 13, 14, 15, 16 for $x = 5.54$, 5.74, 6.80 and 7.20 m, respectively. In each figure: (*a*) gives the ensemble-average surface elevation $\tilde{\eta}$ and $\tilde{\eta} \pm \sigma$, where σ is the standard deviation of the ensemble-average values (obtained for each cycle using the moving-average method); (*b*) gives the ensemble-average, depth-averaged velocity $\tilde{\bar{u}}$ and $\tilde{\bar{u}} \pm \sigma$; (*c*) gives the ensemble-average variation of terms I, II and III from (9) and the overall balance or remainder due to all terms, which is theoretically zero; and (*d*) gives terms IV and V again with the overall balance. It is evident that σ for surface elevation is generally greater than for depth-averaged velocity, supporting the comment about measurement error above. It is also evident that terms I–V have some general similarities, but quite different detailed structures, while the balance term is always very small relative to the maxima, indicating the accuracy of the LDA measurements

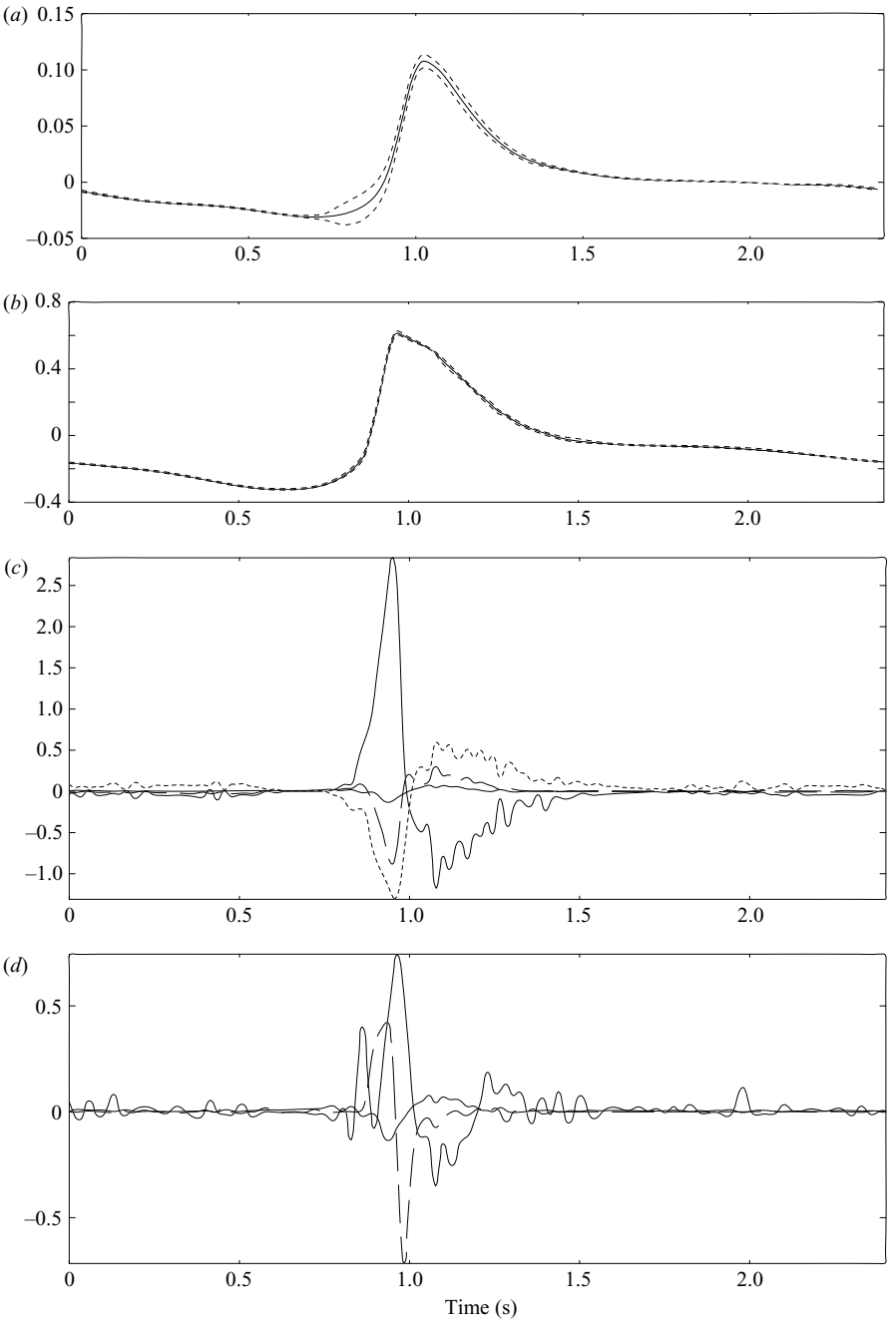

FIGURE 13. Variations of (*a*) surface elevation, (*b*) velocity (both with $\pm$ standard deviation σ shown as dashed lines) and (*c*) momentum terms, —, I; - - -, II; . . . , III, (*d*) —, IV; - - -, V and overall balance with time for position $x = 5.54$ m shown as a full line.

and their subsequent analysis, and also justifying the space–time transformation. Terms VII, VIII and IX are very small and VI is larger, particularly in the initial breaking region. To give a more direct indication of the relative magnitudes of the terms I–V, the r.m.s. values for each position are calculated and plotted against x,

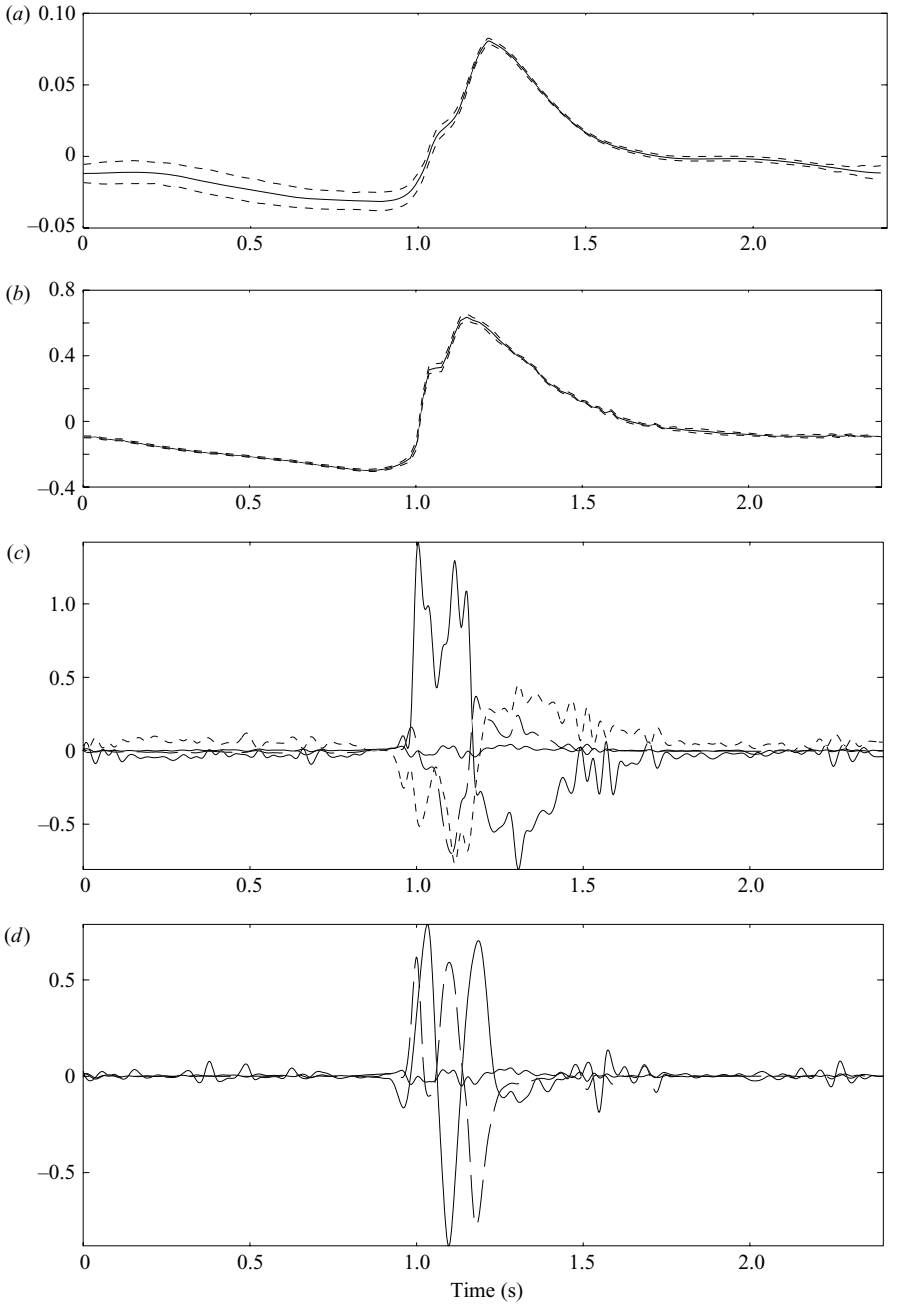

FIGURE 14. As for figure 13, but for $x = 5.74$ m.

the distance from the mid position of the wavemaker, in figure 17. It is shown that term I, the inertia term, is always the largest and the small magnitude of the balance term is clearly apparent. There is considerable variation with x for all terms and the magnitudes of II (advection), III (hydrostatic pressure gradient) and IV (dynamic pressure gradient) and V (vertical dispersion) are always significant, with II and IV smaller for bores than initially. The variation of the terms reflects the rapidly changing

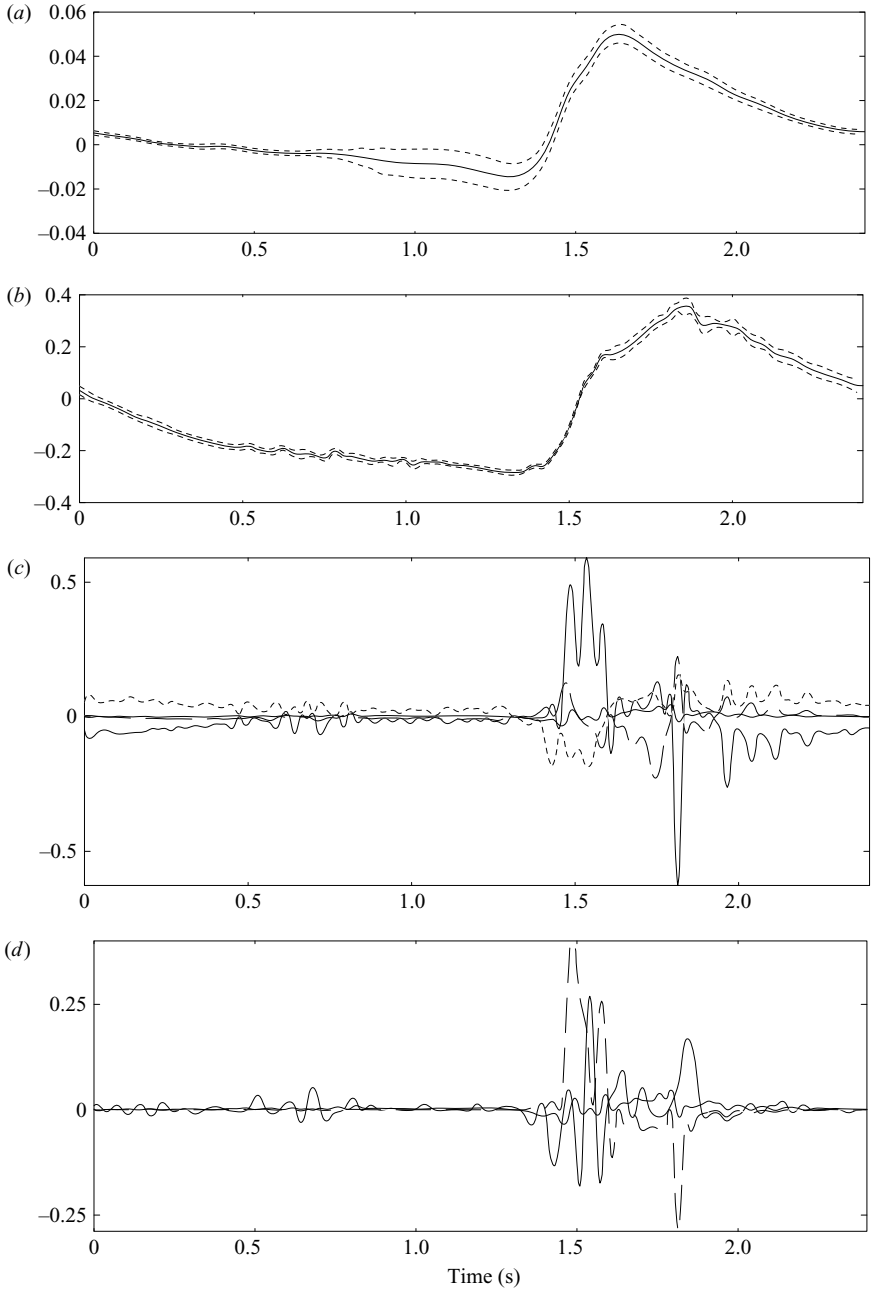

FIGURE 15. As for figure 13, but for $x = 6.80$ m.

nature of the flow and its coherent structures. It should be pointed out that this is a relatively short slope in that the distance from the initial break point to the beach is slightly greater than one wavelength. However, similar complexity was observed by Nadaoka *et al.* (1989) who observed spilling breakers over a horizontal bed region, after a region of bed slope. In order to determine whether the r.m.s. values of 'total' advection, term II–term V, and 'total' pressure gradient, term III–term IV, show similar variability, r.m.s. values are plotted in figure 18. The variability with x is certainly

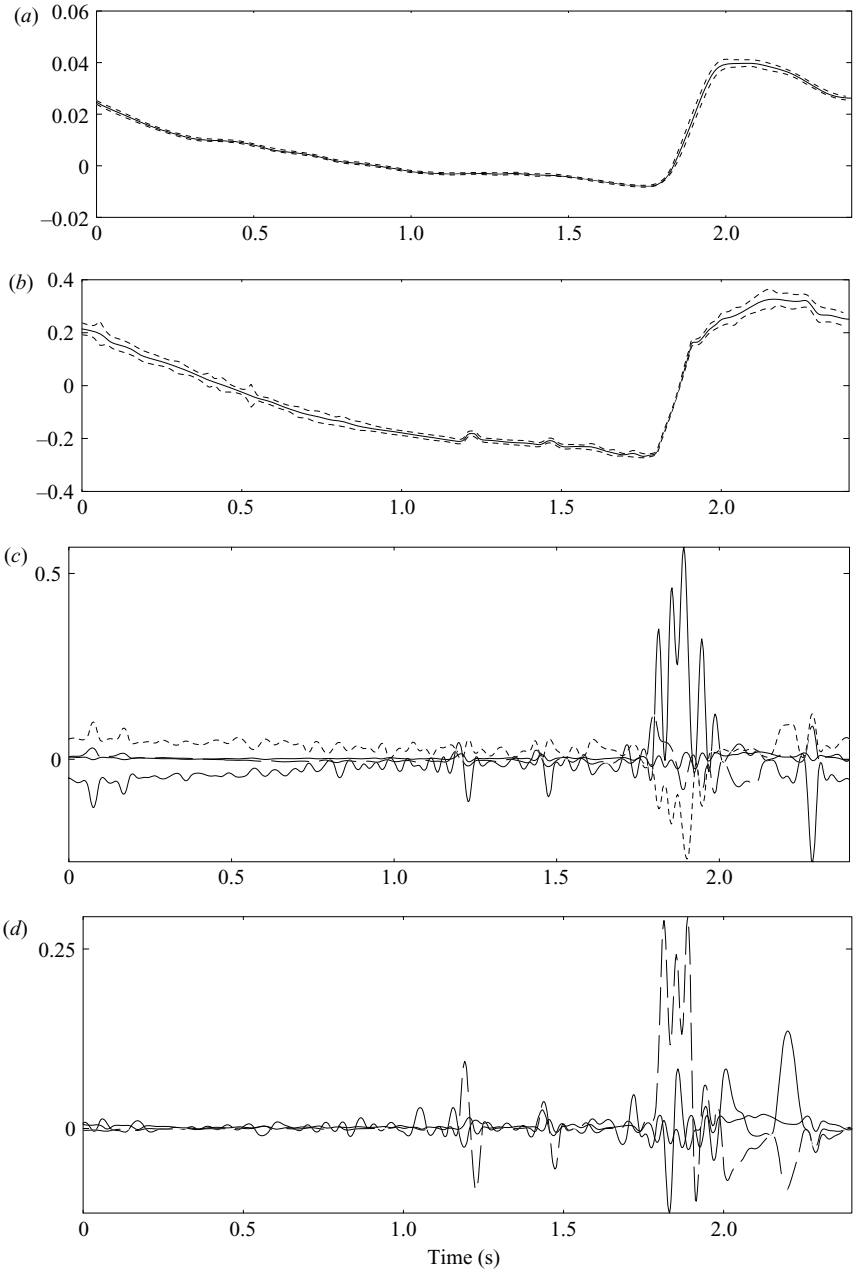

FIGURE 16. As for figure 13, but for $x = 7.20$ m.

less but far from smooth. Finally, r.m.s. values of the Lagrangian acceleration term, $\int_{z_b}^{\tilde{\eta}} D\tilde{u}/Dt \, \mathrm{d}z$, equal to the sum of terms I + II – V, are plotted against x in figure 19 with the total pressure gradient values. The difference is small, as would be expected. The r.m.s. values of residual surface stress term VI is also included as the largest other term; it is noticeable initially, but negligible for bores.

Period-averaged values determine set-up and energy dissipation. However, the period-average of the acceleration term (I in (9)) and the advection terms (II and V),

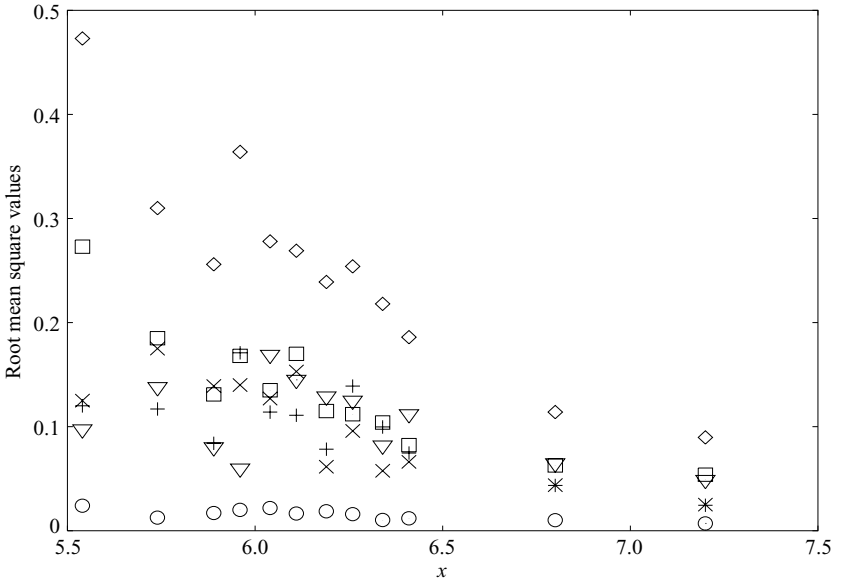

FIGURE 17. Variation of r.m.s. values of terms I (◇), II (+), III (□), IV (×), V (▽) in (9) and overall balance (○), ($m^2\,s^{-2}$), with distance x (m) from the wavemaker.

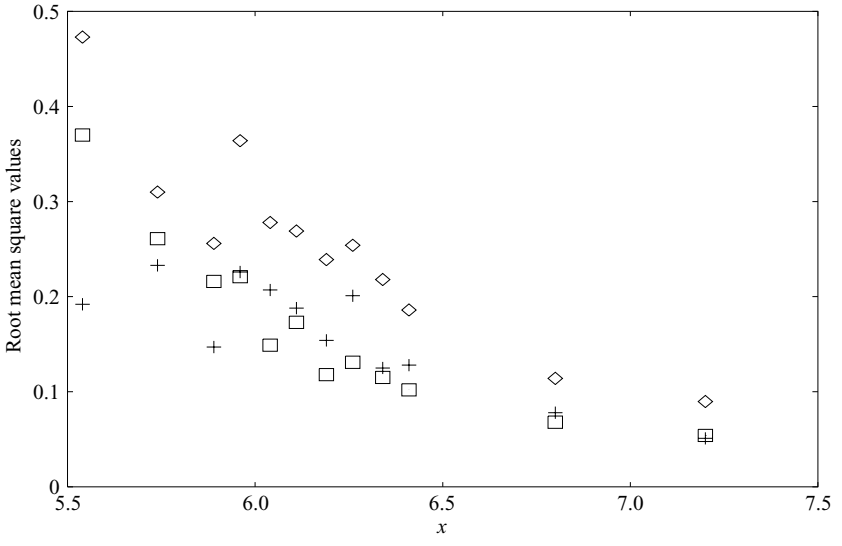

FIGURE 18. Variation of r.m.s. values of terms I (◇), II–V (+), III–IV (□), ($m^2\,s^{-2}$), with distance x (m) from the wavemaker.

after application of the space–time transformation, should be zero and all were of order 1 % of the ensemble-averaged (instantaneous) maximum of the larger terms for a given horizontal location. The period-average of the remainder/balance term was usually about half this. The period-average of the hydrostatic pressure gradient term (III), expected to be non-zero, was usually about 3–4 times higher and the dynamic pressure gradient term (IV) was of similar magnitude. It is thus apparent that the measured data is not sufficiently accurate to give accurate predictions of

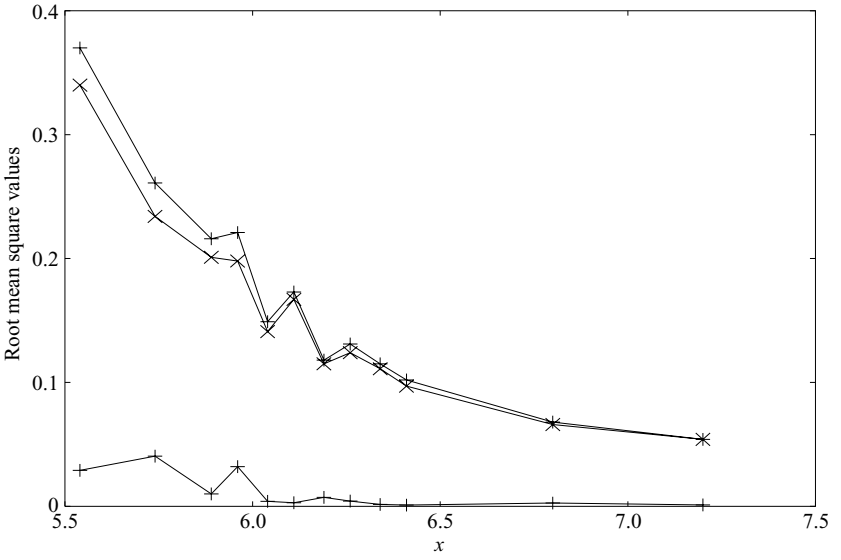

FIGURE 19. Variation of the r.m.s. Lagrangian acceleration term, $\int_{z_b}^{\tilde{\eta}} D\tilde{u}/Dt\,\mathrm{d}z$, I + II – V, (×); r.m.s. 'total' pressure gradient term, III–IV, (+); and the r.m.s. of the surface stress term, VI, (lower +), ($\mathrm{m}^2\,\mathrm{s}^{-2}$) with distance x (m) from the wavemaker.

the small period-averaged quantities. However, given the small magnitudes of the 'instantaneous' remainder term in relation to the maximum values of larger terms, the data with the space–time transformation appears adequate to enable comparison of instantaneous magnitudes of different terms.

6. Shallow-water model results

The model for unsteady bores defined by the shallow-water equations with hydrostatic pressure is described in the Appendix. The measured time history of surface elevation close to the break point, at $x = 4.904$ m, is input. Variation of wave height with x (with $\delta = 0.5$ and friction coefficient $C_f = 0.01$) is compared with experiment in figure 20. A periodic state was reached after about 30 cycles. Agreement in shallow water for bores is quite close, although just after breaking, the shallow-water equations show a greater reduction in wave height than the experiments. Results with $C_f = 0$ were virtually identical. With $\delta = 0$, the bore front was steeper and wave heights in the surf zone were about 20 % higher, but this was partially due to slight over- and undershoot at the bore face; the surface profiles away from the bore front were almost identical. It is shown in figure 21 that r.m.s. values of fluctuating surface elevation, $\tilde{\eta} - \overline{\overline{\eta}}$ where $\overline{\overline{\eta}}$ is the period-averaged value, are less well predicted and the r.m.s. values of depth-averaged velocity, shown in figure 22, are also not so well predicted. One would not expect terms corresponding to the depth-averaged RANS terms to be well predicted as they involve spatial and temporal gradients and will thus be strongly influenced by the steeper fronts in the model.

7. Discussion

This study has concentrated on coherent structures in a two-dimensional vertical plane and it appears that resolution at about the 60th harmonic of the wave frequency

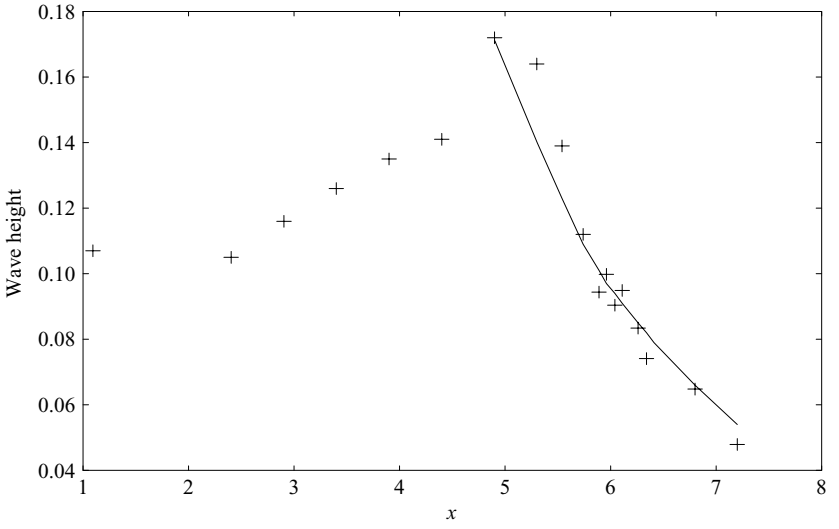

FIGURE 20. Variation of wave height (m) with distance x (m) from the wavemaker: experiments (+) and the shallow-water model (full line).

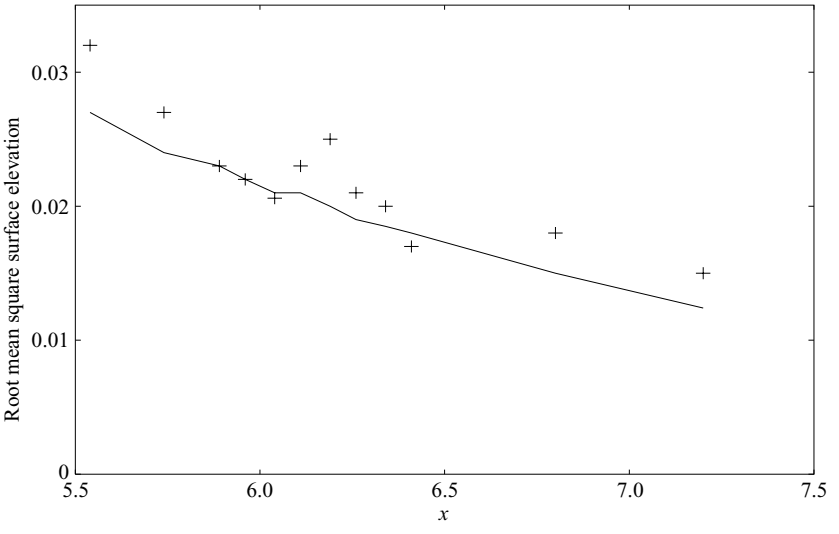

FIGURE 21. Variation of r.m.s. surface elevation fluctuation (m) with distance x (m) from the wavemaker: experiments (+) and the shallow-water model (full line).

is needed. Employing the moving-average method with 120 period divisions and averaging over 375 cycles means that the random turbulence below the 60th harmonic is lost. The velocity spectra with roughly $-5/3$ (log/log) gradients to sometimes as low as the second harmonic support this. However, the characteristics of the relatively high-frequency residual turbulence are of interest. The horizontal and vertical normal Reynolds stresses show quite different behaviour, particularly in the roller region, with the vertical normal stress and the shear stress greatest at the toe of the roller. Isotropy has not been attained in spite of the $-5/3$ spectral gradients (associated with inertia-range isotropic turbulence). Such a high-frequency cut-off is different from previous studies. In hydraulic jump studies, all unsteady motion has been interpreted

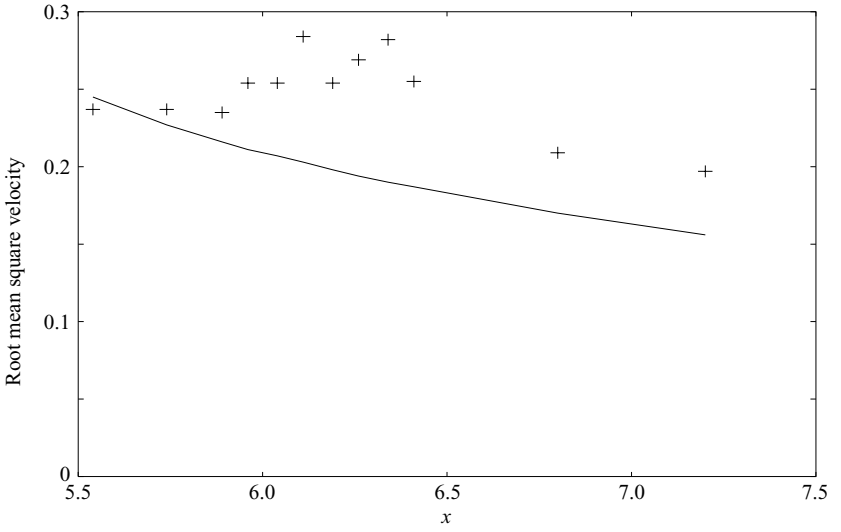

FIGURE 22. Variation of r.m.s. depth-averaged velocity ($m\,s^{-1}$) with distance x (m) from the wavemaker: experiments (+) and the shallow-water model (full line).

as turbulence, as is indeed natural with a steady background flow. Nadaoka *et al.* (1989) had a frequency cut-off at the fifth harmonic. Both cases will include coherent structures, as measured here, as turbulence. Ting & Kirby (1996) employed 'direct' phase-averaging for spilling breakers and also produced spectra with gradients very close to $-5/3$ with 'turbulence' probably also containing coherent structures. These results suggest that a 'clean' definition of turbulence is not possible, at least from single-point velocity measurements; there are no obvious spectral gaps. The coherent vortical structures have length scales varying from greater than the water depth to some fraction of it and turbulence, as identified by the approximate $-5/3$ spectral gradients, overlaps with much of this. Three-dimensional coherent structures, such as obliquely descending vortices, are not even considered. Such overlapping length scales between coherent structures and turbulence would make differentiation using two probes using the approach of Trowbridge & Elgar (2001) impossible, but differentiating between length scales of the order of the wave length (associated with background irrotational motion) and coherent and turbulent structures combined may be possible.

The coherent vortical structures generated during the initial stages of breaking for weakly plunging breakers on a 1:20 slope look qualitatively similar to those of Nadaoka *et al.* (1989) for spilling breakers on a horizontal bed. However, the nature of coherent structures further up the beach are quite different. At the initiation of breaking, the multiple vortical structures last for just over a metre shoreward of breaking, or for about half a period after breaking. Thereafter breakers propagate as bores; an elongated vortical layer along the surface forms in the roller region, with some residual vortical structures shoreward of the roller from the passage of previous bores.

Comparisons have been made with hydraulic jumps. The vorticity maxima which occur near the toe of the roller are similar to hydraulic jump measurements (Svendsen *et al.* 2000) during the initiation of breaking, but decrease markedly soon afterwards. This is presumably due to the mixing and dissipation resulting from the periodic passage of breakers inshore. This obviously does not occur with a hydraulic jump

which is in effect a single stationary event, without upstream turbulence (due to breaking). One might expect spilling breakers to be more similar to hydraulic jumps than plunging breakers which have jet-like impacts on the water below, generating higher vorticity than the more mixing-layer type behaviour of hydraulic jumps and spilling breakers. The weakly plunging breakers here generated slightly higher vorticity maxima than the hydraulic jump values as mentioned above. It is notable that the multiple coherent vortical structures at the initiation of breaking were observed by Yeh & Mok (1990) for hydraulic jumps and Nadaoka *et al.* (1989) for spilling breakers and so are not just prominent for plunging breakers. The important point, however, is that these modify markedly up the slope and become quite different, qualitatively and quantitatively, from hydraulic jumps due to turbulence from previous breakers.

Ting & Kirby (1995, 1996) found that turbulence characteristics for plunging and spilling breakers were quite different. Although multiple coherent structures occur initially for spilling breakers, it may be conjectured that, as breakers become more strongly plunging, the coherent structures propagate further shorewards, producing different turbulence characteristics. However, it has been found that dependence on plunging or spilling does not extend to the swash zone (Cowen *et al.* 2003). Ting & Kirby also show that turbulence is transported shoreward by plunging breakers and seaward by spilling breakers. This could be associated with turbulence being more concentrated in the roller for plunging breakers with prominent shoreward motion and being more distributed for bores, the turbulence outside the roller experiencing seaward motion.

The various terms in the depth-integrated RANS equations show highly irregular (but repetitive) behaviour in the surf zone as might now be expected with complex vortical structures. The residual turbulence makes negligible contribution, and terms due to dynamic pressure and vertical dispersion are as significant as the three terms in the (inviscid) shallow-water equations, with the inertia term always greatest. A solution of these equations, conserving mass and momentum, gave reasonable predictions of wave height variation up the slope, as has been observed by many others. That the mean surface elevation was not well predicted is to be expected as this is due to turbulence and vortical structures which are complex and not represented. The (almost) inviscid equations for momentum conservation have also been shown to give reasonable predictions of run-up due to solitary waves by numerous authors (including Stansby 2003 using the same code) and of overtopping of structures of relatively steep slope (1:2) by Stansby & Feng (2004).

8. Conclusions

Kinematics of surf zone waves have been measured in detail for a particular case with weakly plunging breakers on a 1:20 slope, with an emphasis on determining coherent vortical structures in a vertical plane. These structures are visualized to be of large scale, of the order of the depth, to very small scale and are shown to affect the terms in the depth-integrated RANS equations in a complex irregular manner, with five terms prominent. Vorticity magnitudes are greatest at the toe of the roller and in a non-dimensional form are similar to hydraulic jump values at the initial stages of breaking, but reduce rapidly thereafter. Period-averaged kinematics and vorticity through the surf zone show mean shoreward motion above the trough level and undertow below. There are prominent regions of strong vorticity at trough level at the end of the plunging region, where multiple coherent vortices have dispersed leaving an elongated layer of vorticity along the surface as the bore propagates.

The Reynolds stresses of residual turbulence, which does not include all random motion, are markedly anisotropic although of relatively high frequency. In spite of the complexity of the flow, the inviscid shallow-water equations, which simply conserve mass and momentum, predict the wave height variation up the slope, and indeed have been shown elsewhere to reasonably predict overtopping of sloping sea walls.

It is expected that these conclusions are qualitatively valid for plunging and spilling breakers, as multiple coherent vortices occur during the initiation of breaking to a greater or lesser degree, before propagating as bores and eventually swash. The quantitative details of this particular case should be useful for validating numerical models of general form.

This project was funded as part of EPSRC Grant no. GR/N21741, 'Extreme wave overtopping and flooding at sea defences' at UMIST in parallel with EPSRC Grant no. GR/N22595 involving Alistair Borthwick, Alison Hunt and Paul Taylor at the University of Oxford with whom there has been valuable interaction. The LDA system was provided by the EPSRC equipment loan pool. The referees made numerous helpful suggestions.

Appendix. One-dimensional shallow-water model

The conservation form of the shallow-water equations is used with variables water surface elevation, η, and flux, $h\bar{u}$; u is velocity and the overbar indicates depth-averaged. In one dimension, the depth-averaged continuity and momentum equations are given by:

$$\frac{\partial \eta}{\partial t} + \frac{\partial (h\bar{u})}{\partial x} = 0, \tag{A 1}$$

$$\frac{\partial (h\bar{u})}{\partial t} + \frac{\partial (h\bar{u}^2)}{\partial x} = -gh\frac{\partial \eta}{\partial x} - \frac{\tau_b}{\rho} + \frac{\partial}{\partial x}\left((\nu + \nu_e)\, h\frac{\partial \bar{u}}{\partial x}\right), \tag{A 2}$$

where is ν the kinematic molecular viscosity and ν_e the eddy viscosity. τ_b is the bed shear stress defined by a friction coefficient C_f, such that $\tau_b/\rho = \gamma(h\bar{u})$ with $\gamma = \frac{1}{2}C_f|h\bar{u}/h^2|$. Following the approach in Kennedy *et al.* (2000), the eddy viscosity in the horizontal diffusion term is defined by $\nu_e = \delta^2 h(\partial\eta/\partial t)$ for $\partial\eta/\partial t > 0.15\sqrt{gh}$, with the magnitude linearly increased from zero for $\partial\eta/\partial t > 0.075\sqrt{gh}$. For most cases, $\delta = 0.5$. The numerical solution method is given in Stansby (2003), also in the Appendix of Stansby & Feng (2004).

The seaward input is defined by the measured time variation of surface elevation at the break point. The computational domain extends seaward of this point and outward travelling waves are absorbed using a sponge layer.

REFERENCES

Battjes, J. A. 1974 Surf similarity. *Proc. 14th Intl Conf. Coastal Engng ASCE*, pp. 466–480.

Brocchini, M. & Peregrine, D. H. 2001 The dynamics of strong turbulence at free surfaces. Part 2. Free-surface boundary conditions. *J. Fluid Mech.* **449**, 255–290.

Christiensen, E. D. & Deigaard, R. 2001 Large eddy simulation of breaking waves. *Coastal Engng* **42**, 53–86.

Cowen, E. A., Sou, I. M., Liu, L. F. & Raubenheimer, B. 2003 PIV measurements within a laboratory generated swash zone. *ASCE J. Engng Mech.* **129**, 1119–1129.

Cox, D. T. & Anderson, S. L. 2001 Statistics of intermittent surf zone turbulence and observations of large eddies using PIV. *Coastal Engng* **43**, 121–131.

Cox, D. T., Kobayashi, N. & Okayasu, A. 1994 Vertical variations of fluid velocities and shear stress in surf zones. *Proc. 24th Intl Conf. Coastal Engng ASCE* pp. 98–112.

Cox, D. T. & Kobayashi, N. 2000 Identification of intense, intermittent coherent motions under shoaling and breaking waves. *J. Geophys. Res.* **105**(C6), 14 223–14 236.

Dodd, N. 1998 Numerical model of wave run-up, overtopping and regeneration. *J. Waterway, Port, Coastal Ocean Engng, ASCE* **124**, 73–81.

Hibberd, S. & Peregrine, D. H. 1979 Surf and runup on a beach: a uniform bore. *J. Fluid Mech.* **95**, 323–345.

Kennedy, A. B., Chen, Q., Kirby, J. T. & Dalrymple, R. A. 2000 Boussinesq modelling of wave transformation, breaking and runup. I:1-D. *J. Waterway, Port, Coastal Ocean Engng ASCE* **126**, 39–47.

Lesieur, M. 1990 *Turbulence in Fluids*, 2nd edn. Kluwer.

Lin, P. & Liu, P. L.-F. 1998 A numerical study of breaking waves in the surf zone. *J. Fluid Mech.* **359**, 239–264.

Liu, M., Rajaratnam, N. & Zhu, D. Z. 2004 Turbulence structure of hydraulic jumps of low Froude number. *J. Hydr. Engng ASCE* **130**, 511–520.

Madsen, P. A., Bingham, H. B. & Liu, H. 2002 A new Boussinesq method for fully nonlinear waves from shallow to deep water. *J. Fluid Mech.* **462**, 1–30.

Madsen, P. A., Sorensen, O. R. & Schäffer, H. A. 1997 Surf zone dynamics simulated by a Boussinesq type model. Part I. Model description and cross-shore motion of regular waves. *Coastal Engng* **32**, 255–287.

Nadaoka, K., Hino, M. & Koyano, Y. 1989 Structure of the turbulent flow field under breaking waves in the surf zone. *J. Fluid Mech.* **204**, 359–387.

Nezu, I. & Nakagawa, H. 1993 *Turbulence in Open Channel Flows*. IAHR Monograph Series, A. A. Balkema, Rotterdam, Netherlands.

Peregrine, D. H. 1967 Long waves on a beach. *J. Fluid Mech.* **27**, 815–827.

Peregrine, D. H. & Svendsen, I. A. 1978 Spilling breakers, bores and hydraulic jumps. *Proc. 16th Intl Conf. Coast. Engng ASCE*, pp. 540–550.

Qiao, H. & Duncan, J. H. 2001 Gentle spilling breakers: crest flow-field evolution. *J. Fluid Mech.* **439**, 57–85.

Schäffer, H. A., Madsen, P. A. & Deigaard, R. 1993 A Boussinesq model for waves breaking in shallow water. *Coastal Engng* **20**, 185–202.

Stansby, P. K. 2003 Solitary wave runup and overtopping by a semi-implicit finite-volume shallow-water Boussinesq model. *J. Hydraul Res.* **41**, 639–648.

Stansby, P. K. & Feng, T. 2004 Surf zone wave overtopping a trapezoidal structure: 1-D modelling and PIV comparison. *Coastal Engng* **51**, 483–500.

Stive, M. J. F. 1984 Energy dissipation in waves breaking on gentle slopes. *Coastal Engng* **8**, 99–127.

Svendsen, I. A., Veeramony, J., Bakunin, J. & Kirby, J. T. 2000 The flow in weak turbulent hydraulic jumps. *J. Fluid Mech.* **418**, 25–57.

Ting, C. K. T. & Kirby, J. T. 1994 Observations of undertow and turbulence in a laboratory wave flume. *Coastal Engng* **24**, 51–80.

Ting, C. K. T. & Kirby, J. T. 1995 Dynamics of surf-zone turbulence in a strong plunging breaker. *Coastal Engng* **24**, 177–204.

Ting, C. K. T. & Kirby, J. T. 1996 Dynamics of surf-zone turbulence in a spilling breaker. *Coastal Engng* **27**, 131–160.

Toro, E. F. 2001 Shock-capturing methods for free-surface shallow flows. Wiley.

Trowbridge, J. & Elgar, S. 2001 Turbulence measurements in the surf zone. *J. Phys. Oceanogr.* **31**, 2403–2417.

Veeramony, J. & Svendsen, I. B. 2000 The flow in surf zone waves. *Coastal Engng* **39**, 93–122.

Yeh, H. H. & Mok, K. M. 1990 On turbulence in bores. *Phys. Fluids* A **2**, 821–828.

Zelt, J. A. 1991 The runup of nonbreaking and breaking solitary waves. *Coastal Engng* **15**, 205–246.